ISRSSP 2013

Third International Symposium on

Radio Systems and Space Plasma

Proceedings

28 -29 August, 2013 • Sofia, Bulgaria

Organized by: JCREST

In Cooperation with: AMAKOTA

Under the Auspices of URSI

ISRSSP 2013

PROCEEDINGS

of the Third International Symposium
on Radio Systems and Space Plasma

Sofia, Bulgaria
28-29 August, 2013

Organized by

IICREST - Interdisciplinary Institute for Collaboration and Research on Enterprise Systems and Technology

In Cooperation with

Aristotle University of Thessaloniki
AMAKOTA Ltd.

Under the Auspices of

URSI – International Union of Radio Science

Edited by Blagovest Shishkov

Graphics Production by Canka Petrova

Printed in Bulgaria

ISBN: 978-619-90124-1-3

http://www.isrssp.org

secretariat@iicrest.org

BRIEF CONTENTS

KEYNOTE SPEAKER

Blagovest Shishkov

Bulgarian Academy of Sciences

Bulgaria

CHAIR AND PROGRAM COMMITTEE

CHAIR

Blagovest SHISHKOV, Bulgarian Academy of Sciences, Bulgaria

PROGRAM COMMITTEE

Jorgen Bach ANDERSEN, Aalborg University, Denmark

A.K.M. BAKI, Independent University of Bangladesh, Bangladesh

Maurice BELLANGER, CNAM, France

Jun CHENG, Doshisha University, Japan

Peter DAVIS, ATR, Japan

Hristo KABAKCHIEV, Sofia University St. Kl. Ohridski, Bulgaria

Pierre KAUFMANN, Mackenzie Presbyterian University, Brazil

Hirotsugu KOJIMA, Kyoto University, Japan

Andon LAZAROV, Burgas Free University, Bulgaria

Francoise LEFEUVRE, LPCE/CNRS, France

Frank LITTLE, Texas A & M University, USA

Vladimir LYUBCHENKO, Russian Academy of Sciences, Russia

Marin NENCHEV, Technical University - Sofia, Bulgaria

Yoshiharu OMURA, Kyoto University, Japan

Petko PETKOV, Technical University - Sofia, Bulgaria

Michel PARROT, LPCE/CNRS, France

Bodo REINISCH, University of Massachusetts - Lowell, USA

Michael RUDERMAN, University of Sheffield, UK

Tapan SARKAR, Syracuse University, USA

Naoki SHINOHARA, Kyoto University, Japan

Tadashi TAKANO, Nihon University, Japan

Hideyuki USUI, Kobe University, Japan

Madalina VLAD, Association EURATOM/MEdC, Romania

Andrzej WERNIK, Polish Academy of Sciences, Poland

Alexander SHMELEV, Radiotechnical Institute by Acad. A.L.Mints, Russia

Angela SLAVOVA, Bulgarian Academy of Sciences, Bulgaria

FOREWORD

This book contains the proceedings of ISRSSP 2013 – the Third International Symposium on Radio Systems and Space Plasma, held in Sofia, Bulgaria on June 28-29, 2013. The proceedings consist of 10 high-quality research and experience papers that have not been published previously.

The Symposium was organized by the Interdisciplinary Institute for Collaboration and Research on Enterprise Systems and Technology (IICREST) under the auspices of the International Union of Radio Science (URSI), in cooperation with Aristotle University of Thessaloniki and AMAKOTA Ltd.

The symposium is focusing on Radio Systems and Space Plasma, considering the following research areas:

(i) Radio Communication Systems and Signal Processing;

(ii) Satellite Space Observations;

(iii) Trans-Ionospheric Propagation;

(iv) Space Plasma, Waves, and Particles;

(v) Solar Power Satellite (SPS) Systems.

as announced in the ISRSSP'13 Call for Papers. These areas are relevant to the work in several URSI Commissions, namely: Commission C – (i), Commission G – (ii), Commission F – (iii), and Commission H – (iv). We nevertheless focus not only on foundational topics that concern the above-mentioned areas but also on more application-oriented research relevant to the areas – this may include Space Applications, Power Transmission, and so on. The papers in the current proceedings are mainly in areas (i), (ii), and (v); most of the papers present foundational research and several papers are more applications-oriented. This inspires us to work harder for attracting more contributions that touch upon Trans-Ionospheric Propagation and Space Plasma, Waves, and Particles.

ISRSSP aims at more than just serving as dissemination platform for URSI-related research. ISRSSP has its own original profile and we work to spread its influence to a broader audience including all those researchers and practitioners who are interested in the particular topics selection of the symposium. We are inspired to go forward with this event, contributing to the dissemination of radio science -related knowledge.

FOREWORD (CONT.)

With regard to this nevertheless, we also aim at reinforcing the influence and quality of all our URSI-related dissemination activities and they include not only the current symposium but also the International Conference on Telecommunications and Remote Sensing – these both events are organized and sponsored by IICREST. The areas of ISRSSP and ICTRS are close, though not overlapping. Still, we observe that many members of our research Community are interested in both events. Hence, in order to facilitate them in attending these events, we are going for CO-LOCATING as from 2014 both events: ICTRS and ISRSSP. They would become part of a joint conference on Telecommunications but still they will of course preserve their identities. For this reason, we are inviting all of you to consider participating next year in the joint ISRSSP-ICTRS event!

With regard to ISRSSP'13, the high quality of the program is enhanced by a Keynote Lecture and informal discussions that complement the 10 paper presentations. These high points in the symposium program would contribute to positioning ISRSSP as a high quality event, especially in the light with the future co-location with ICTRS.

Building an interesting and successful program for the symposium required the dedicated efforts of many people. We must thank the authors, whose research efforts are recorded here and also the Program Committee – for supporting the paper selection and the promotion of the event. We would like to especially thank IICREST and AMAKOTA for taking care of the organization, realizing a brilliant organizational set up. We would be happy if IICREST continues organizing ISRSSP (and ICTRS), under the auspices of URSI. And last but not least, we would like to especially compliment Canka Petrova who has not only compiled the current proceedings but has also performed numerous organizational activities, on behalf of IICREST.

We wish you all an inspiring symposium and enjoyable stay in the beautiful city of Sofia. We look forward to seeing you next year in Luxembourg, for the Fourth International Symposium on Radio Systems and Space Plasma (ISRSSP 2014) which (as mentioned already) will be co-located with ICTRS 2014. You may find details on the websites of the events: http://www.isrssp.org and http://www.ictrs.org.

Blagovest Shishkov

Chair of ISRSSP 2013

CONTENTS

KEYNOTE SPEAKER

On the Minimization of Side-Lobes in Large Antenna Arrays for Microwave Power Transmission

Blagovest Shishkov

Institute of Mathematics & Informatics, Bulgarian Academy of Sciences,
Acad. G. Bonchev Str. Bl.8, Sofia 1113, Bulgaria
bshishkov@math.bas.bg

Abstract: Recent advances in space exploration have shown a great need for antennas with high resolution, high gain and low side lobe level (SLL). The last characteristic is of paramount importance especially for the Microwave Power Transmission (MPT) in order to achieve higher transmitting efficiency (TE). In order to achieve low side lobe levels, statistical methods play an important role. Various interesting properties of a large antenna array with randomly, uniformly and combined spacing of elements have been studied, especially the relationship between the required number of elements and their appropriate spacing from one viewpoint and the desired SLL, the aperture dimension, the beamwidth and TE from the other. We propose a new unified approach in searching for reducing SLL by exploiting the interaction of deterministic and stochastic workspaces of proposed algorithms. Our theoretic study and simulation results clarify how to deal with the problem of side lobes in designing a large antenna array, which seems to be an important step toward the realization of future SPS/MPT systems.

Keywords: Microwave power transmission; Large antenna array; Uniform spacing; Random spacing; Spatial and amplitude tapering; Side lobe level; Grating lobes; Workspace; Transmitting efficiency.

BRIEF BIOGRAPHY

Prof. D.Sc. Blagovest Shishkov received his Ph.D. degree in Physics from the Institute of Electronics, Bulgarian Academy of Sciences and his D.Sc. degree from the Technical University of Sofia, Bulgaria, in 1974 and 1991 respectively. Presently he is professor emeritus at Institute of Mathematics and Informatics, Bulgarian Academy of Sciences.

He has published more than hundred research papers and three books in Signals Transmission (Signals, Filtering and Detection) and especially asymptotic methods in parameter estimation, signal detection and identification, pattern recognition and data quantization.

His latest investigations and results are connected by signal processing of cyclostationary signals and detecting and studying of nonlinear wave interactions by using higher-order statistics. Both areas are successfully incorporated into adaptive antenna beamforming and analysis of time series associated with space data. He was Visiting Professor in Japan (seven times), France (three times), Spain and etc.

He is / used to be member of IEEE, EURASIP, IEICE, numerous PCs of international Conferences.

He is President of the Bulgarian URSI Committee and acts as a Program Chair and PC member and reviewer for several international conferences.

PAPERS

Active Integrated Antennas and Arrays with Field-Effect Transistors

Vladimir E. Lyubchenko

Fryazino branch of Kotelnikov Institute of Radioengineering and Electronics,
Russian Academy of Sciences. 141190, Moscow Rgn., Fryazino, Vvedensky sq. 1, Russia.
lyubch@ire216.msk.su

Abstract. Electromagnetic wave generation processes in the hybrid log-periodic microstrip antenna on the dielectric substrate integrated with field-effect transistor are experimentally studied in the frequency range of 6–20 GHz. The possibility of synchronization and power combining in the array of antenna-coupled oscillators is investigated. It is shown that considerable increasing of generation efficiency and power combining can be obtained by using the external synchronization signal or quasi-optical design of the array.

1. Introduction

Active antennas or antenna-oscillators are simple and compact radiators that can be applied in microwave and millimeter wave frequency ranges as the elements of arrays [1, 2]. Investigation of the generation processes and power combining in active antenna arrays shows the advantages of field-effect transistors in such applications [3]. In this work, the log-periodic planar antennas with field-effect transistors are studied. Mutual and external synchronization of the oscillators are used for increasing the generation efficiency and space power combining.

2. Log-periodic active antenna

Depending on the antenna-coupled oscillator application, different types of the planar antennas can be used. For the broad frequency band operation, log-periodical antennas are of the interest. Using of the dielectric substrate with metallized back side provides the necessary level of the feedback for microwave generation. The log-periodic active antenna structure which was used in this work is shown in Fig. 1, where d is the substrate thickness; l is the tooth length.

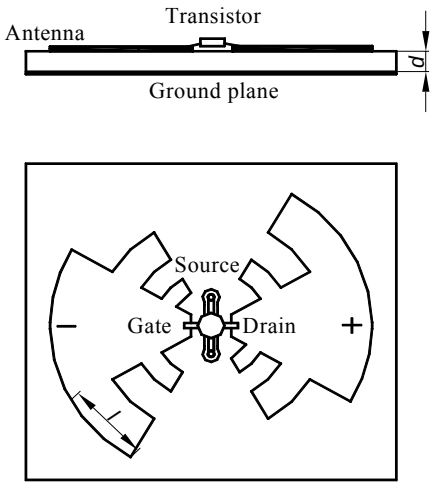

Fig. 1. Log-periodic active antenna with field-effect transistor (cross-section and top view)

This antenna can be represented as a set of the resonant circuits with frequencies $f_1(\sqrt{2})^n$, where f_1 is the antenna fundamental frequency defined by the length of largest tooth; $n = 0,1,2,3,...$ At the fundamental frequency, such radiator has a sufficiently high quality factor exceeding 100. Computer modeling and experimental research of the electromagnetic field parameters were performed to optimize the design and to estimate the prospective of log-periodic antennas application in antenna arrays and power combiners. The fundamental frequency is defined by the length of the largest tooth l approximately equal to a quarter of the effective wavelength

$$l \approx \lambda_{eff} / 4;\ \lambda_{eff} = \lambda_0 / \sqrt{(\varepsilon + 1)/2}\ .$$

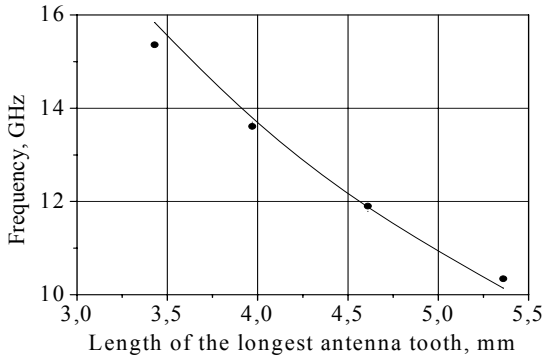

Fig. 2. Oscillation frequency of the active antenna as a function of its geometry: solid curve – the results of calculation; experimental data are depicted by points.

Fig. 2. shows, that the calculated oscillation frequencies of the active antenna are in good agreement with measured results

As a multi-resonance system, the log-periodic antenna can operate in multi-frequency mode. Here, the dependence of the transistor gain versus the operating frequency plays the key role. In our research we have explored the field-effect transistor NE350184C with the gain dependence shown in Fig. 3.

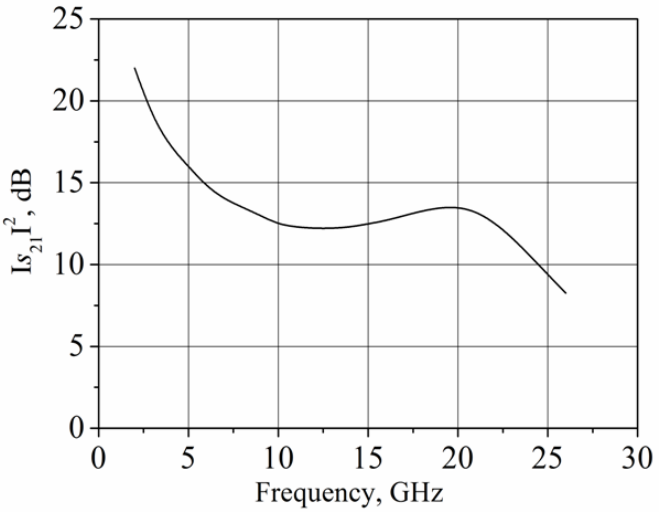

Fig. 3. The gain of the NE350184C field-effect transistor versus operating frequency

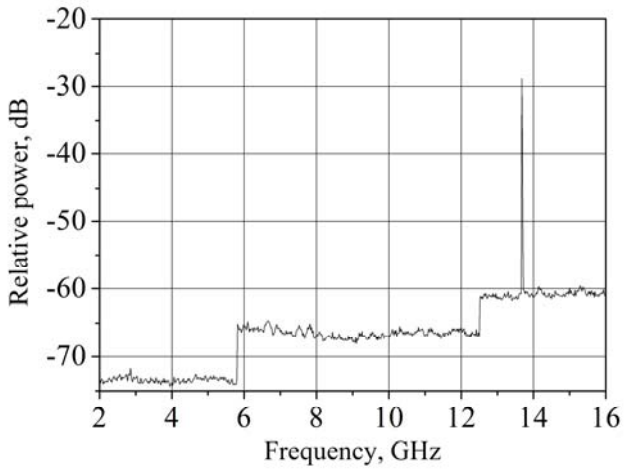

Fig. 4. The radiation spectrum of the active antenna in a single-frequency mode

Fig. 4 represents the signal spectrum of the antenna designed on the dielectric substrate with thickness $d = 0.2\lambda_d$ close to quarter wavelength on the fundamental frequency. The measured oscillation frequency is close to the predicted value and is equal to $f_{1c} = 13.7$ GHz.

3. Synchronization and space power combining of the active antenna radiation

The active antenna described above can be employed as a radiating element in the quasi-optical array. In this case it is important to provide the frequency and phase synchronization of the antenna-coupled oscillators disposed on the common dielectric substrate. The experimental data [4-6] show that mutual synchronization of the antenna-coupled oscillators is possible, if the discrepancy between their operation frequencies is less than 50 MHz. Mutual influence of the oscillators occurs due to the excitation of the surface waves in the dielectric substrate. Irradiation of the array by the external microwave source offers more opportunities of the frequency and phase synchronizations for a large number of independent oscillators. Frequency range, in which the synchronization occurs at the operation frequency of external oscillator, depends on the number of antenna-oscillators in the array and the intensity of the external irradiation as it is shown at Fig. 5.

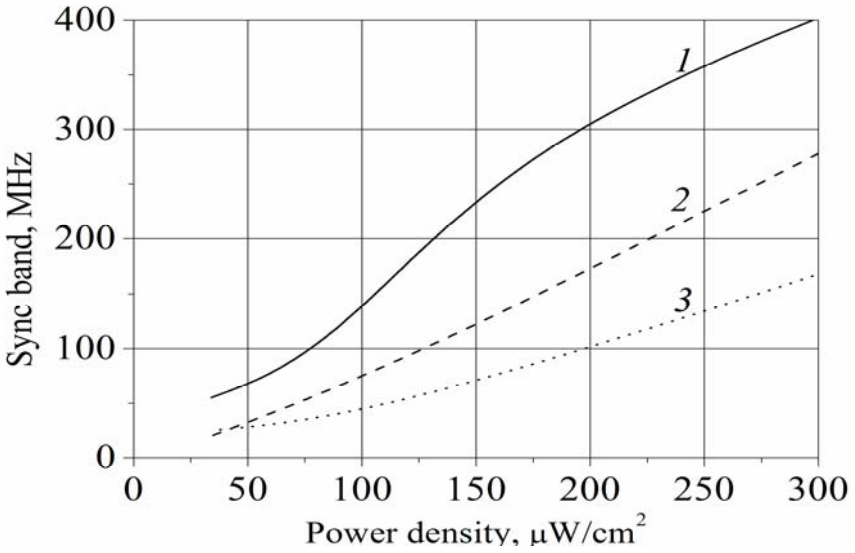

Fig. 5. The width of external synchronization band for single active antenna (*1*) as well as for linear arrays consisting of two (*2*) and three (*3*) mutually synchronized antenna-oscillators versus the power flow density of the external signal

As follows from this figure, increasing the number of simultaneously operating active antennas leads to decreasing the band of their synchronization by external signal. The synchronization band monotonically grows with the increase of the power flow density of the external electromagnetic field. The power level, necessary for the external synchronization, is much less than the output power of the array.

4. Synchronization of the array in the quasi-optical resonator

The possibility of increasing the interaction between active antennas by applying the quasi-optical resonator was also investigated to increase the mutual synchronization band. If the dielectric reflector is located near antenna array parallel to its plane as in [3], the mutual synchronization frequency band of active antennas can reach the value of 140 MHz. Radiation patterns of the array consisting of three active antennas are shown in Fig. 6 for the case when the differences in their own frequencies are ~100 MHz. The graph *1* represents the radiation pattern of array in which the active antennas are not mutually synchronized. The curve *3* depicts the radiation pattern of array consisted of the active antennas which are effectively synchronized in presence of the reflector. The shape of radiation pattern in the case of absence of the reflector under conditions of mutual synchronization is shown by curve*2*.

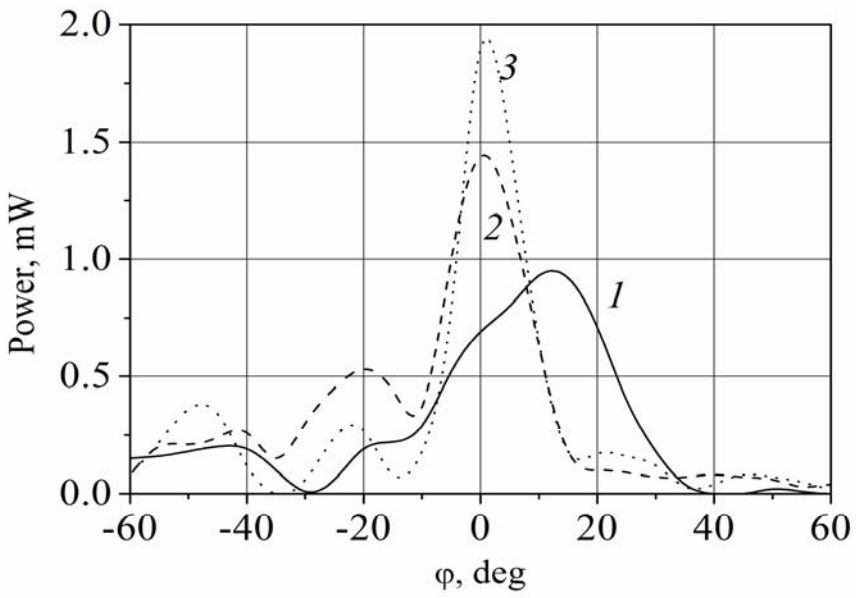

Fig. 6. Radiation patterns of the linear array consisting of four antenna-oscillators for the case when active antennas are: (*1*) not synchronized; (*2*) mutually synchronized; (*3*) synchronized with external irradiation

Log-periodic planar antenna integrated with field-effect transistor is a compact and effective source of electromagnetic wave radiation in the wide frequency range. Such oscillators can be used as active elements of antenna arrays. Mutual and external synchronization are used for increasing the generation efficiency and space power combining. More details are in the recent publications [4,5].

References

1. V.E. Lyubchenko (Ed), The Science and Technology of Millimetre Wave Components and Devices. ─ London ─ New York: Tailor & Francis, pp.34-38, 2002.
2. K. Chang, R. A.York, P. S. Hall, T. Itoh, "Active integrated antennas", IEEE Transactions on Microwave Theory and Techniques, vol. 50, pp. 937─944, March 2002.
3. R. A. York, R. C. Compton, "Quasi-optical power combining using mutually synchronized oscillator arrays", IEEE Transactions on Microwave Theory and Techniques, vol. 39, pp.1000─1009, June 1991.
4. V. E. Lyubchenko, V. D. Kotov, E. O. Yunevich, "Active microstrip antenna with Gann diode", Radiophysics and Quantum Electronics, vol. 46, pp. 799─803, Aug.-Sept. 2003.
5. V. I. Kalinin, V. D. Kotov, V. E. Lyubchenko, E. O. Yunevich, "Synchronization and combining of the radiation powers of active microwave antennas integrated with field-effect transistors", Journal of Communications Technology and Electronics, vol. 55, pp. 934─937, August 2010.

BSAR Geometry, Range Resolution Determination and Signal Modeling

Andon Dimitrov Lazarov[1], Todor Kostadinov[2], Dimitar Minchev[1], and José Passos Morgado[(3)]

[1] BFU, 62 San Stefano Str, 8000 Burgas, Bulgaria,
{labaro, mitko}@bfu.bg

[2] IICT, BAS, Acad. G. Bonchev Str., bl. 25-A, 1113 Sofia, Bulgaria,
kostadinov.todor@yahoo.com

[3]Air Force Academy, Lisbon, Portugal,
japmorgado@gmail.com

Abstract. Two classes of Bistatic Synthetic Aperture Radar (BSAR) are considered: topology with transmitter of opportunity moving target and stationary receiver so called BGISAR, and topology with stationary transmitter and receiver and moving target, so called BFISAR. BSAR geometry and kinematical equations and are defined. Mathematical models of the deterministic BSAR signal are created based on phase code modulated signals. The expression of time dependent BSAR range resolution is derived. Image reconstruction procedures with different types of emitted signals are defined. The effectiveness of models and algorithms are illustrated with results of numerical experiments.

1. Introduction

For last ten years Bistatic Synthetic Aperture Radar (BSAR) technique attracts intensive research interest [1 ÷ 3]. In [4] bistatic concept in SAR application for Earth observation is analyzed. Prospective and problems in space-surface bistatic synthetic aperture radar are described in [5]. Bistatic SAR concept with application to moving target detection is discussed in [6]. A new topology for a sub-class of bistatic SAR, called Space-Surface Bistatic SAR (SS-BSAR) that comprises Global Navigation Satellite Systems (GNSS) as transmitters of opportunity and a stationary receiver on the ground is presented in [7]. Several BSAR signal processing techniques for image reconstruction have been proposed [8-10] that provide effective tools for radar imaging of cooperative targets. Effects of bistatic configurations on ISAR imaging have been largely investigated in [11, 12].

Two classes of BSAR systems are of particular interest, the class of with non-cooperative transmitter that comprises a spaceborne transmitter, and a receiver which is located on the Earth and the class with stationary transmitter and receiver. The main problems to be solved are to describe the BGISAR and BFISAR geometries, GPS – C/A and P phase code modulating waveforms and based on it to derive a signal model and image reconstruction procedure, as well as to describe the time dependent BSAR

range and Doppler resolutions. The rest of the paper is organized as follows. Section 2 describes BSAR topologies and kinematic equations. Section 3 is dedicated to BSAR GPS phase code modulated transmitted pulse and 3-D BSAR signal models. Section 4 illustrates BSAR image reconstruction procedure. In Section 5 results of the numerical experiment are presented

2. BSAR Topology and Kinematic Equations

2.1. BGISAR Geometry

Bistatic Generalize Inverse Synthetic Aperture Radar (BGISAR) scenario is illustrated in Fig. 1. GPS transmitter, receiver located on the land surface and a target flying helicopter are all situated in Cartesian coordinate system *Oxyz*, where $\mathbf{R}^s(p)$ is the current position vector of the transmitter in discrete time instant p, $\mathbf{R}_{00'}(p)$ is the current position vector of the mass center of the target, $\mathbf{R}^r$ is the stationary position vector of the receiver. The target presented as an assembly of point scatterers is depicted in Cartesian coordinate system *OXYZ*, where $\mathbf{R}_{ijk}$ is the position vector of the *ijk*th point scatterer.

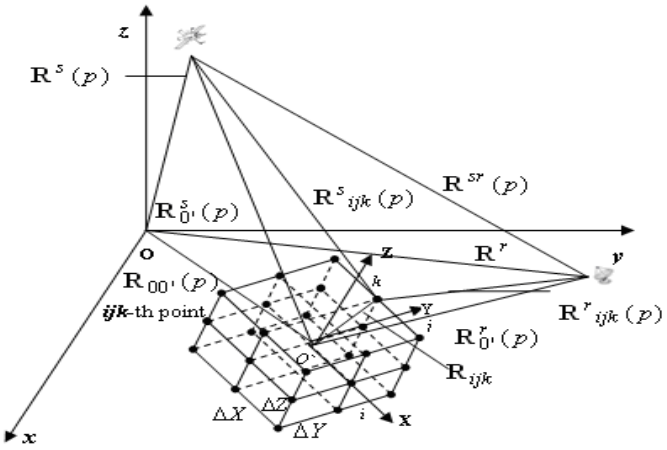

Fig. 1. BGISAR geometry.

The position vector of the target's mass center with respect to the transmitter, $\mathbf{R}^s_{0'}(p)$ is defined by

$$\mathbf{R}^s_{0'}(p) = \mathbf{R}^s(p) - \mathbf{R}_{00'}(p) = \mathbf{R}^s - \mathbf{R}_{00'}(0) - \mathbf{V}\left(\frac{N}{2} - p\right)T_p, \quad (1)$$

where $\mathbf{V}$ is the velocity vector of the target, $p=\overline{1,N}$ is the current number of the emitted pulse, N is the full number of emitted pulses, T_p is the registration time interval (time acquisition interval), (pT_p) is the discrete slow time.

The position vector of the target's mass center with respect to the receiver, $\mathbf{R}^r_{0'}(p)$ is defined by

$$\mathbf{R}^r_{0'}(p)=\mathbf{R}^r-\mathbf{R}_{00'}(p)=\mathbf{R}^r-R_{00'}-\mathbf{V}\left(\frac{N}{2}-p\right)T_p. \tag{2}$$

The position vector of the *ijk*th point scatterer with respect to the transmitter, $\mathbf{R}^s{}_{ijk}(p)$ is defined by

$$\mathbf{R}^s{}_{ijk}(p)=\mathbf{R}^s_{0'}(p)+\mathbf{AR}_{ijk}=\mathbf{R}^s_{0'}(p)-\mathbf{R}_{00'}(0)-\mathbf{V}\left(\frac{N}{2}-p\right)T_p+\mathbf{AR}_{ijk}. \tag{3}$$

The calculation of the elements of the transition matrix $\mathbf{A}$ can be found in [13]. The position vector of the *ijk*th point scatterer with respect to the receiver, $\mathbf{R}^s{}_{ijk}(p)$ is defined by

$$\mathbf{R}^r{}_{ijk}(p)=\mathbf{R}^r_{0'}(p)-\mathbf{AR}_{ijk}=\mathbf{R}^r-\mathbf{R}_{00'}(0)-\mathbf{V}\left(\frac{N}{2}-p\right)T_p-\mathbf{AR}_{ijk}. \tag{4}$$

The round trip distance from GPS transmitter to the target and GPS receiver is defined by

$$R_{ijk}(p)=\left|\mathbf{R}^s{}_{ijk}(p)\right|+\left|\mathbf{R}^r{}_{ijk}(p)\right|. \tag{5}$$

Expressions (1-5) are applied in modeling of BGISAR signal.

2.2. BFISAR Geometry

The geometry of Bistatic Forward Inverse Synthetic Aperture Radar BFISAR topology is presented in Fig. 2. Consider UWB stationary transmitter and receiver both located on the land or sea surface and as a mariner target a ship all situated in a Cartesian coordinate system *Oxyz*. The target presented as an assembly of point scatterers is depicted in its own coordinate system *OXYZ*. Vectors $\mathbf{R}^s$ and $\mathbf{R}^r$ are the position vectors of the transmitter and receiver respectively in a coordinate system *Oxyz*.

The vector $\mathbf{R}_{ijk}$ is the position vector of *ijk*-th point scatterer in the coordinate system *OXYZ* and $\mathbf{R}_{00}(p)$ is the current position vector of the mass center of the target at the time instant *p*. Based on the geometry in Fig. 2 the following kinematical vector equations hold. Range distance vector from the transmitter to the mass center of the target

$$\mathbf{R}^s(p)=\mathbf{R}^s-\mathbf{R}_{00}(p)=\mathbf{R}^s-\mathbf{R}_{00}(0)-\mathbf{V}\left(\frac{N}{2}-p\right)T_p, \tag{6}$$

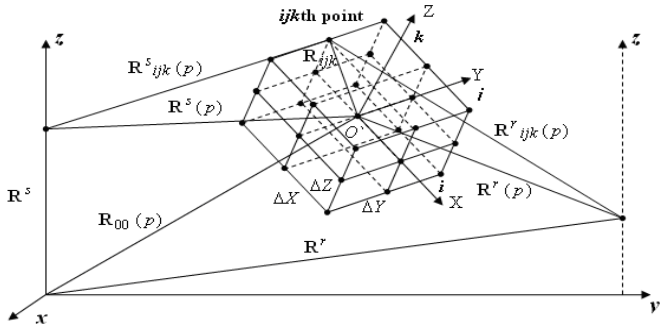

Fig. 2. BFISAR geometry

where **V** is the target's velocity vector, *N* is the full number of emitted pulses, T_p is the time acquisition interval. Range distance vector from the mass center of the target to the receiver

$$\mathbf{R}^r(p) = \mathbf{R}^r - \mathbf{R}_{00}(p) = \mathbf{R}^r - R_{00}(0) - \mathbf{V}\left(\frac{N}{2} - p\right)T_p . \tag{7}$$

Range distance vector from the transmitter to the *ijk*th point scatterer of the target

$$\mathbf{R}^S{}_{ijk}(p) = \mathbf{R}^S(p) + \mathbf{A}\mathbf{R}_{ijk} = \mathbf{R}^S - \mathbf{R}_{00}(0) - \mathbf{V}\left(\frac{N}{2} - p\right)T_p + \mathbf{A}\mathbf{R}_{ijk} , \tag{8}$$

where **A** is the coordinate transformation matrix. In case the axes OZ and $O'z$ are collinear, then

$$\mathbf{A} = \begin{bmatrix} \cos\alpha & \sin\alpha & 0 \\ -\sin\alpha & \cos\alpha & 0 \\ 0 & 0 & 1 \end{bmatrix},$$

where α is the vector velocity guiding angle, defined between $O'X$ and Ox axes. Range distance vector from the *ijk*th point scatterer of the target to the receiver

$$\mathbf{R}^r{}_{ijk}(p) = \mathbf{R}^r(p) - \mathbf{A}\mathbf{R}_{ijk} = \mathbf{R}^r - \mathbf{R}_{00}(0) - \mathbf{V}\left(\frac{N}{2} - p\right)T_p - \mathbf{A}\mathbf{R}_{ijk} . \tag{9}$$

The round trip range distance transmitter- *ijk*th point scatterer of target-receiver is defined by

$$R_{ijk}(p) = \left|\mathbf{R}^S{}_{ijk}(p)\right| + \left|\mathbf{R}^r{}_{ijk}(p)\right| . \tag{10}$$

Expressions (6-10) are applied in modeling of BFISAR signal.

2.3. BSAR Range Resolution

Consider a plane defined by transmitter, point like target and receiver, described in two dimensional coordinate system (2-D) (Fig. 2), where *A* is the position of the transmitter, *B* is the position of the receiver, and *T* is the position of the target. Denote $AT = R_A$ and $TB = R_B$. The constant phase of a transmitter-target-receiver signal is proportional to the sum of distances transmitter-target and target-receiver,

i.e. $R_A + R_B = L + 2.i.(\Delta R)$ = const, the equation of ellipses, where $AB = L$ is the distance between transmitter and receiver, the base line, $i = 1, 2, \ldots$ is the index of the equal distance ellipse, $\Delta R = c/(2.\Delta F)$ is the quasi mono static range resolution, defined by the bandwidth ΔF of the emitted signal and the speed of the light $c = 3.10^8$ m/s.

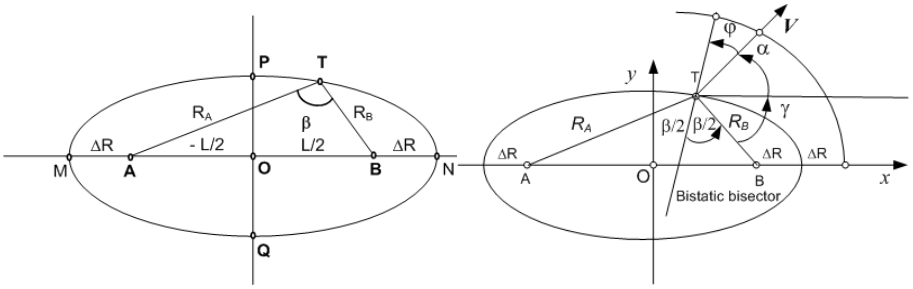

(*a*) (*b*)

Fig. 3. BSAR Geometry (*a*) and definition of angles (β/2), γ, α, and φ in BSAR geometry (*b*).

The lines of a constant range $R_A + R_B$ (transmitter-target-receiver) or the lines of zero Doppler coincide with concentric ellipses with focal points R_A and R_B. The space between two consecutive ellipses defines a range resolution cell. According to [15] the range resolution cell's width depends on the bistatic angle and/or bisector's direction, and angle shift φ in respect of a bistatic bisector inside the range resolution cell (Fig. 3), and is defined by the expression

$$\Delta R_\varphi \approx \frac{(\Delta R)}{\cos(\beta/2)\cos\varphi}. \tag{11}$$

The lines of the constant range difference (R_A - R_B), i.e. of the maximum bistatic target Doppler are orthogonal to the ellipses of a constant range $R_A + R_B$, and described by hyperbolas with the focal points that coincide with the foci of the ellipses. The bisector of the bistatic angle at any point on an ellipse is perpendicular to the tangent of the ellipse, and hence collinear with the tangent of the corresponding hyperbola. If the angle of the target velocity vector in respect of bistatic bisector is φ (Fig. 3, *b*), the Doppler frequency is described by the expression [15],

$$F_D = 2\frac{V}{\lambda}\cos(\beta/2)\cos\varphi. \tag{12}$$

where V is the target velocity, λ is the wavelength, $\varphi = \pi - [(\beta/2) + \gamma + \alpha]$, α is the target velocity angle.

The angle γ can be defined by analytical geometrical relationships in Fig. 3, where the coordinates of the transmitter, point **A** are (-(L/2), 0), the coordinates of the receiver, point **B** are ((L/2), 0), and the coordinates of the target, point **T** are $[x(t), y(t)]$. Assume the target is moving rectilinearly at a constant vector-velocity **V.** Then the target trajectory is described with following equations

$$x(t) = x_0 + V_x t,\ y(t) = y_0 + V_y t, \tag{13}$$

where $V_x = V\cos\alpha$, and $V_y = V\sin\alpha$ are the coordinates of the vector velocity, x_0 and y_0 are the initial coordinates of the target. The equation of line *BT* can be described as

$$\frac{x-(L/2)}{x(t)-(L/2)} = \frac{y}{y(t)} \tag{14}$$

Then the angle γ between *BT* and the auxiliary line parallel to *Ox* axis is a function of time and defined by the expression

$$\gamma(t) = \arctan\frac{y(t)}{(L/2)-x(t)}. \tag{15}$$

Based on the movement of the target, the angle β becomes a function of time and is defined by a cosine theorem in the triangle *ABT*, i.e.

$$\beta(t) = \arccos\left(\frac{R_A^2(t)+R_B^2(t)-L^2}{2R_A(t)R_B(t)}\right). \tag{16}$$

The time dependent quantities in (16) are defined by following expressions

$$R_A(t) = \sqrt{\left(\frac{L}{2}\right)^2 + L.x(t) + x^2(t) + y^2(t)},\ R_B(t) = \sqrt{\left(\frac{L}{2}\right)^2 - L.x(t) + x^2(t) + y^2(t)}. \tag{17}$$

The expression (16) can be written as

$$\beta(t) = \arccos\left(\frac{R^2(t)-(L/2)^2}{\sqrt{\left[(L/2)^2+R^2(t)\right]^2 - L^2x^2(t)}}\right),\quad R^2(t) = \left(x_0+V_xt\right)^2 + \left(y_0+V_yt\right)^2 \tag{18}$$

2.4. BSAR Doppler resolution

BSAR Doppler resolution is defined by the value of the coherent processing time, called integration time, and can be expressed as $\Delta F_D = 1/\hat{T}$, where ΔF_D is the Doppler resolution, $\hat{T}$ is the coherent processing time.

3. BSAR GPS Phase Code Modulated Transmitted Pulse and 3-D BSAR Signal Models

Assume GPS transmitter illuminates the target by a sequence of phase code modulated pulse trains. Each phase code modulated pulse train is described as

$$S(t) = a.\mathbf{rect}\left(\frac{t}{T}\right)\exp\{-j[\omega t + \pi b(t) + \varphi_0]\}, \tag{19}$$

where a is the intensity of the pulse train, $\omega = 2\pi c / \lambda$ is the angular frequency, φ_0 is the initial phase, $c = 3.10^8$ m/s is the velocity of the light, $b(t)$ is the binary parameter of the phase code modulated pulse train, defined by coefficients of polynomials as follows.

3.1. C/A - GPS Phase Code

Tapped Feedback Shift Registers (TFSRs) are used to generate a sequence of "0"s and "1"s of the C/A (coarse acquisition) code at the clock rate of 1.023 MHz. At each clock pulse the bits in the registers are shifted to the right where the content of the rightmost register is read as output. A new value in the leftmost register is created by the modulo-2 addition (or binary sum) of the contents of a specified group of registers.

Two 10-bit TFSRs are used, each generating a Gold Code:

- Code G_1 presented as the polynomial: $1 + X^3 + X^{10}$,
- Code G_2 presented as the polynomial: $1 + X^2 + X^3 + X^6 + X^8 + X^9 + X^{10}$.

The output of the G1 (rightmost register) is modulo-2 added to the register contents of the G2. Different combinations of the outputs of the registers of G2 (or "taps" from the register) when added to the output of the G1 code lead to different pseudo random noise (PRN) codes. There are 36 unique codes that can be generated in such a manner. For example: PRN1 taps the contents of register 2 and 6, and adds it to the output of the G1 TFSR, PRN2 taps the contents of register 3 and 7, PRN3 taps the contents of register 4 and 8, and so on. Corresponding to the figure above tap 1 is used in the numerical experiments.

3.2. P - GPS Phase Code

Assume GPS transmitter emits *P* (precision) code sequence on a carrier frequency L1=1575.42 MHz with a chipping rate $(10.23).10^6$, and period of $6.1871.10^{12}$ chips, generated by four 12-bit shift registers designated by X1A, X1B, X2A, and X2B. The function of the registers is described by the polynomials [14]

X1A:$1 + X^6 + X^8 + X^{11} + X^{12}$; X1B:$1 + X^1 + X^2 + X^5 + X^8 + X^9 + X^{10} + X^{11} + X^{12}$;

X2A:$1 + X^1 + X^3 + X^4 + X^5 + X^7 + X^8 + X^9 + X^{10} + X^{11} + X^{12}$; X2B:$1 + X^2 + X^3 + X^4 + X^8 + X^9 + X^{12}$

Initial states of the registers:

X1A: 001001001000; X1B: 010101010100; X2A: 100100100101; X2B: 010101010100.

Consider a GPS transmitter illuminating a target with a *K*-chip segment of *P* phase code modulated waveform. Then each *P* phase code modulated segment can be expressed by (23), where $T = 13/(10.23.10^6)$ s is the time duration of the segment, $b(t)$ is the time binary sequence that modulates the phase of the GPS signal. For (*K*=13)-chip segment $b(t)$ accepts values: 1001001001000. The transmitter's signal power is -163 dBW, and receiver peak power is -120 dBm. Signal power density of the satellite transmitter on the Earth is $3.0628.10^{-14}$ W/m^2. The receiver to target range varies in the interval 100-1000 m.

3.3. GPS Phase Code Modulated BSAR signal model

The deterministic component of the BSAR signal return reflected by ijk th point scatterer is defined by

$$S_{ijk}(p,t) = a_{ijk}\,\mathbf{rect}\frac{t-t_{ijk}(p)}{T}\,\mathbf{exp}\left\{-j\left[\omega(t-t_{ijk}(p))+\pi b(t)\right]\right\} \tag{20}$$

$$\mathbf{rect}\frac{t-t_{ijk}(p)}{T} = \begin{cases} 1, \text{ if } 0 \le \dfrac{t-t_{ijk}(p)}{T} < 1; \\ 0, \text{ if } \dfrac{t-t_{ijk}(p)}{T} < 0 \text{ and } \dfrac{t-t_{ijk}(p)}{T} \ge 1; \end{cases} \tag{21}$$

a_{ijk} is the reflective coefficient of the ijkth point scatterer, three-dimensional (3-D) image function; T is the time duration of the C/A phase code, $t_{ijk}(p) = \dfrac{R_{ijk}(p)}{c}$ is the round trip delay to ijk th point scatterer; $t = t_{ijk\,\min}(p) + (k-1)\Delta T$, ΔT is the time duration of the phase segment, $k = \overline{1, L+K-1}$ is the current number of segment, $\Delta T = (10.23).10^{-6}$ s is the chip time duration for P code, $K = T/\Delta T = 1023$ is the full number of segments of the C/A phase code, $K = T/\Delta T = 13$ is the full number of chips in the P phase code segment, $L = \mathbf{int}\left[\dfrac{t_{ijk\,\max}(p) - t_{ijk\,\min}(p)}{\Delta T}\right]$ is the relative dimension of the target, $t_{ijk\,\min}(p) = \dfrac{R_{ijk\,\min}(p)}{c}$ and $t_{ijk\,\max}(p) = \dfrac{R_{ijk\,\max}(p)}{c}$ are minimal and maximal round time delay, respectively.

The deterministic component of the BSAR signal, reflected by all point scatterers from the object surface for every p th GPS C/A and P pulse train has the form

$$S(p,t) = \sum_{ijk} a_{ijk}\,\mathbf{rect}\frac{t-t_{ijk}(p)}{T}\,\mathbf{exp}\left\{-j\left[\omega(t-t_{ijk}(p))+\pi b(t)\right]\right\}. \tag{22}$$

which in discrete form can be written as [13]

$$S(p,k) = \sum_{ijk} a_{ijk}\,\mathbf{rect}\frac{\hat{t}_{ijk}^{\hat{k}}(p)}{T}.\mathbf{exp}\left\{-j\left[\omega(t_{ijk\,\min}(p)+(k-1)\Delta T - t_{ijk}^{\hat{k}}(p)) + \pi b((k-\hat{k}+1)\Delta T)\right]\right\} \tag{23}$$

where $\hat{t}_{ijk}^{\hat{k}}(p) = t_{ijk\,\min}(p) + (k-1)\Delta T - t_{ijk}^{\hat{k}}(p)$, $\hat{k}$ denotes a current number k while the function $\mathbf{rect}(.)$ for a particular $t_{ijk}(p)$ accepts value 1 first time and can be considered as a projective discrete coordinate of ijkth point scatterer on the range direction. It is possible for many time delays, $t_{ijk}(p)$ the parameter $\hat{k}$ to accept value 1. The expressions (24)÷(27) can be used to model GPS C/A and P phase code

modulated BGISAR signal return in case the object is moving on a rectilinear trajectory in 3-D coordinate system.

4. BSAR Image Reconstruction Procedure

The phase demodulated BSAR signal has the form

$$\hat{S}(p,k)=\sum_{ijk} a_{ijk}\,\mathbf{rect}\frac{\hat{t}_{ijk}^{\hat{k}}(p)}{T}\,\mathbf{exp}\left\{-j\left[\omega(t_{ijk\,\min}(p)-t_{ijk}^{\hat{k}}(p))+\pi b((k-\hat{k}+1)\Delta T)\right]\right\}. \quad (24)$$

Equation (24) is a space transform from three-dimensional image function (3-D) into two-dimensional (2-D) signal plane. Then the 2-D projection of the 3-D image function on the range and azimuth direction $a_{ijk}(\hat{p},\hat{k})$ can be extracted from (11) by inverse space transform form from 2-D signal plane into 2-D image space, i.e.

$$a_{ijk}(\hat{p},\hat{k})= \sum_{p=\overline{1,N}}\sum_{k=\hat{k}}^{\hat{k}+K-1}\left[\hat{S}(p,k)\exp j[\pi b((k-\hat{k}+1)\Delta T)]\right]..\mathbf{exp}\left\{j\omega\left[t_{ijk\,\min}(p)-t_{ijk}^{\hat{k}}(p)\right]\right\} \quad (25)$$

Tailor expansion of $\omega[t_{ijk\,\min}(p)-t_{ijk}^{\hat{k}}(p)]$ yields

$$\omega[t_{ijk\,\min}(p)-t_{ijk}^{\hat{k}}(p)]=\frac{2\pi}{N}\hat{p}.p+\Phi(p),\ \Phi(p)=a_2(pT_p)^2+...+a_m(pT_p)^m \quad (26)$$

is the phase term of higher order, $\hat{p}$ is the azimuth coordinate of *ijk*th scatterer. Then the equation (25) can be rewritten as

$$a_{ijk}(\hat{p},\hat{k})= \sum_{p=\overline{1,N}}\left\{\sum_{k=\hat{k}}^{\hat{k}+K-1}\left[\hat{S}(p,k).\mathbf{exp}(j\Phi(p))\right].\mathbf{exp}[j\pi b((k-\hat{k}+1)\Delta T)]\right\}.\mathbf{exp}\left\{j\left[\frac{2\pi}{N}\hat{p}p\right]\right\} \quad (27)$$

Accordingly, the algorithm of the 2-D complex image extraction includes the following operations:

1. Higher order phase correction (motion compensation) by the expression

$$\widetilde{S}(p,k)=\hat{S}(p,k).\mathbf{exp}(j\Phi(p)). \quad (28)$$

Definition of exact values of the polynomial coefficients of $\Phi(p)$ is an optimization iteration procedure [13].

2. Range compression by cross-correlation

$$\widetilde{S}(\hat{p},\hat{k})=\sum_{k=\hat{k}}^{\hat{k}+K-1}\widetilde{S}(p,k)\mathbf{exp}[j\pi b((k-\hat{k}+1)\Delta T)], \quad (29)$$

where $\hat{k}$ is the discrete coordinate of *ijk*th point scatterer on the range direction.

3. Azimuth compression (complex image extraction) by inverse Fourier transformation

$$a_{ijk}(\hat{p},\hat{k}) = \sum_{p=\overline{1,N}} \widetilde{S}(p,\hat{k})\mathbf{exp}\left\{ j\left[\frac{2\pi}{N}\hat{p}p \right] \right\}. \qquad (30)$$

5. Numerical experiment

A numerical experiment has been carried out to verify the 3-D geometry of the scenario and model of BSAR signal with GPS P code phase modulation and to prove the correctness of the developed digital signal image reconstruction procedure. It is assumed that the target, a flying helicopter is moving rectilinearly in a 3-D Cartesian coordinate system of observation $Oxyz$. GPS transmitter transmits a P code train.

Coordinates of the GPS satellite at the moment $p = N/2$: $x^s = 1{,}5.10^4$ m, $y^s = 2.10^4$ m; $z^s = 2.10^5$ m.GPS satellite velocity $v_x^s = 3819{,}206$ m/s, $v_y^s = 3819{,}206$ m/s, $v_z^s = 0$ m/s. Coordinates of the stationary GPS receiver: $x^r = 970$ m, $y^r = 10^3$ m and $z^r = 30$ m. The trajectory parameters of the target: velocity $V = 80$ m/s; guiding angles $\alpha = \pi/4$, $\beta = \pi/4$, $\gamma = 3\pi/2$; coordinates of the target's mass-centre at the moment $p = N/2$: $x_{00} = 20$ m, $y_{00} = 10$ m, $z_{00} = 150$ m. Parameters of the GPS P phase code waveform: wavelength $\lambda = 19{,}1.10^{-2}$ m, frequency $f = 1.57.10^9$ Hz, number of GPS P chips in the segment $K = 13$, range sample number 256, GPS P phase code segments number during aperture synthesis $N = 512$, time acquisition interval $T_p = 10^{-2}$ s. The geometry of the helicopter is depicted in a 3-D coordinate grid with cell's dimensions ΔX=ΔY=ΔZ=1m. Numerical results are presented in Figs. 4 and 5. Based on (23) real and imaginary parts of a BSAR signal are calculated and presented in Fig. 4.

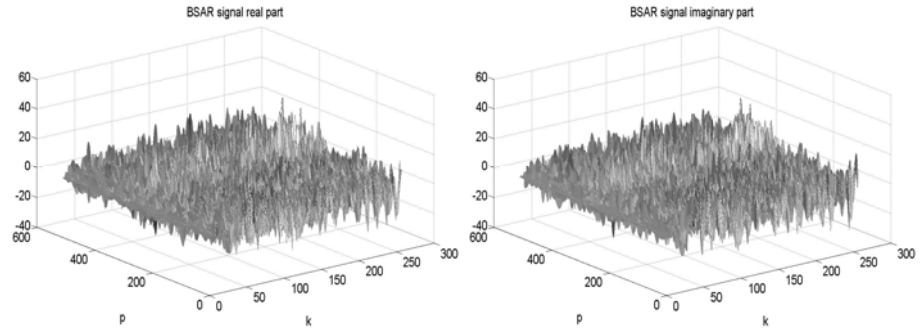

Fig. 4. BSAR signal (real part nad imaginary part).

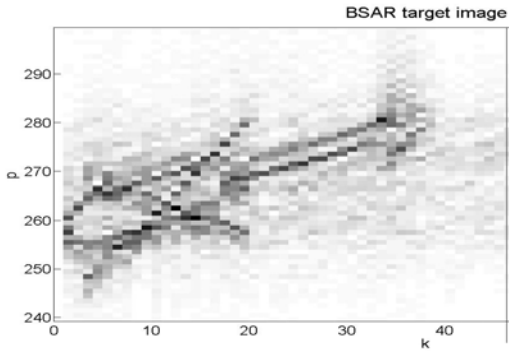

Fig. 5. BSAR image of the helicopter.

The final BSAR image of a helicopter after all stages of signal modeling and image reconstruction is depicted in Fig. 5. The quality of imaging is satisfactory, which can be regarded as illustration of range resolution capabilities of a GPS *P* phase code waveform and its BSAR application.

6. Conclusion

In the paper BSAR geometry with GPS transmitter of opportunity, moving target and receiver is described. The BSAR time dependent range resolution has been derived. Deterministic BSAR signal model based on GPS C/A and P code modulated waveforms has been defined. All stages of image reconstruction, including phase correction, cross-correlation range compression and azimuth compression by Fourier transform have been defined. Numerical experiment has been carried out in order to illustrate effectiveness of the signal modeling and target imaging by GPS P code modulated waveforms.

Acknowledgment

This paper is supported by MEYS, BSF, the project DTK 02/28.2009, DDVU 02/50/2010

References

1. M. Cherniakov (ed.), “Bistatic Radar: Emerging Technologies”, Wiley-Interscience, 2008.
2. A.P. Whitewood, C.J. Baker, H.D. Griffiths, “Bistatic radar using a spaceborne illuminator”, IEE international radar conference, Edinburgh, October 2007.
3. J. Sanz-Marcos, P. Prats, J.J. Mallorqui, A. Aguasca, “A sub-aperture range-doppler processor for bistatic fixed-receiver SAR”, EUSAR, May 2006.

4. Moccia, Rufmo, G., D'Errico, M., Alberti, G., et. al. “BISSAT: A bistatic SAR for Earth observation”, Proc. of IEEE International Geoscience and Remote Sensing Symposium (IGARSS'02), Vol. 5, June 24-28, 2002, pp. 2628-2630.
5. M. Cherniakov, “Space-surface bistatic synthetic aperture radar Prospective and problems”, Proc. of International Conference of Radar-2002, Edinburgh, UK, 2002, pp. 22-26.
6. Whitewood A., Muller B., Griffiths H., and Baker, C. “Bistatic SAR with application to moving target detection”, Proc. of International Conference RADAR-2003, Adelaide, Australia, 2003.
7. M. Cherniakov, E. Plakidis, M. Antoniou, R. Zuo, “Passive space-surface bistatic SAR for local area monitoring: Primary feasibility study”, Proc. of the 6th European Radar Conference, EuMA, 30Sept- 2Oct. 2009, Rome, Italy, pp 89-92.
8. O. Loffeld, Nies, H., Peters, V., and S. Knedlik, “Models and useful relations for bistatic SAR processing”, Proceedings of International Geoscience and Remote Sensing Symposium (IGARSS), vol. 3, Toulouse, France, July 21-25, 2003, pp. 1442 - 1445.
9. J. H. G. Ender, I. Walterscheid, and A. R. Brenner,“New aspects of bistatic SAR: Processing and experiments”, 2004 Proceedings of International Geoscience and Remote Sensing Symposium (IGARSS), vol. 3, Anchorage, AK, Sept. 20 - 24, 2004, pp. 1758 - 1762.
10. D. D’Aria, A. M. Guarnieri, and F. Rocca, “Focusing bistatic synthetic aperture radar using dip move out”, IEEE Transactions on Geoscience and Remote Sensing, 42, no. 7, 2004, pp. 1362 - 1376.
11. M. Martorella, J. Palmer, J.Homer, Br. Littleton, and D. Longstaff, “On bistatic inverse synthetic aperture Radar”, IEEE, Transaction on Aerospace Electronic System, vol. 43, no. 3, July 2007, pp. 1125-1134.
12. F.Berizzi, and Dalle Mese, “E. Sea-wave fractal spectrum for SAR remote sensing”, IEE Proc. Radar, Sonar and Navigation, 148, no. 2, 2001, pp. 56-66.
13. A.D. Lazarov, “Digital Image Processing, ISAR Signal Formation and Image Reconstruction as Complex Spatial Transforms”, Ch. 2, InTech, 2011, pp 27-50. ISBN 978-953-307-801-4
14. Domenik Farmer, Kreg Martin, Patent No 5202604, Apr 13 1993.
15. Nicholas J. Willis, "Bistatic Radar, Second Edition" Publisher: SciTech, 2005.

Multi-Band RF Circuits for Future Mobile Terminals

Hiroshi Okazaki, Takayuki Furuta, Kunihiro Kawai, Yuta Takagi,
Atsushi Fukuda, and Shoichi Narahashi

NTT DOCOMO, INC., 3-6 Hikarino-oka, Yokosuka, Kanagawa, 239-8536, Japan,
{okazakih,furutat,kawaikun,takagiyu,fukudaat,narahashi}
@nttdocomo.co.jp

Abstract. Multi-band radio frequency (RF) circuits will be a predominant solution for future global and compact mobile terminals, which supports several cellular systems, such as the Global System for Mobile communications, the third generation, and the Long Term Evolution in various frequency bands. A single-path configuration and use of single-band devices with distributed reconfigurable matching networks have the potential to achieve the optimum RF front-end for future multi-mode multi-band mobile terminals. A power amplifier (PA) is one of the key components in the RF front-end because its power consumption affects operating time of the terminal. Considering the difficulties in configuring a practical tunable band-pass filter as a top filter or duplexer, collaboration between the filter and low-noise amplifier is a candidate to achieve the performance level required for the RF front-end. This paper overviews the recent progress in our research on the multi-band circuits. These RF circuits will contribute to the multi-mode band-free operation in future mobile terminals.

1. Introduction

Mobile terminals are expected to have multi-mode and multi-band operation capabilities to be able to connect from anywhere with adequate bit rate. With regard to frequency bands for cellular systems, the number of frequency bands required for a global mobile terminal is 4 for the Global System for Mobile communications, 3-5 for the third generation (3G) cellular system. The number for the Long Term Evolution (LTE) and/or WiMAX will be increased to 12-14 [1]. A Radio frequency (RF) front-end (RF-FE) in the mobile terminal should cover these vast number of frequency bands. In conventional cellular phones, multiple power amplifier(s) (PA(s)), filters, and low noise amplifier(s) (LNA(s)) are installed for multi-band use, as shown in Fig.1. RF integrated circuit (RFIC) generally includes most of RF functions except PA, duplexer, band-pass filter (BPF) and antenna switch, and may have transceivers for other wireless systems such as Wireless Local Area Network, and receivers for the Global Positioning System and/or Digital Video Broadcasting.

In the conventional RF-FE configuration, the most suitable circuit combination is selected from among several built-in circuits with the frequency band selection.

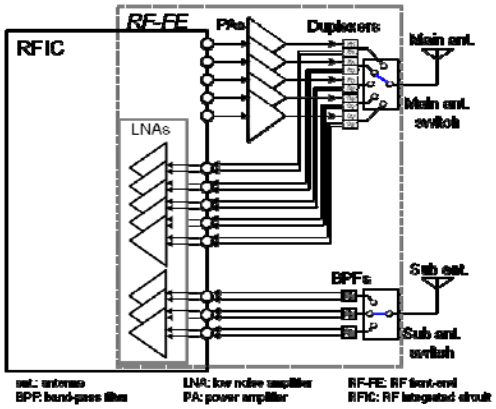

Fig.1. Block diagram example of RF front-end in a conventional cellular phone

The RF-FE shown in Fig. 1 can process 5 different frequency bands for 3G and/or LTE, and also have a diversity or 2-stream multiple-input and multiple-output (MIMO) receiving capability at 3 out of the 5 bands by using a sub receiver. However, the terminal handling *m* bands and *n* spatial streams for MIMO should have (*m* x *n*) transceivers. In the case of 12-band and 4-stream MIMO, the terminal should have 48 transceivers. Therefore, there have been a lot of studies of achieving multi-band or broadband circuits that comprise a compact and cost-effective multi-band RF-FE with adequate RF performance [2-3]. Broadband technique is not suitable for PAs and filters because of performance issues. A reconfigurable or tunable technique for RF circuits seems to be a way to provide a compact multi-band RF-FE that supports a large number of frequency bands.

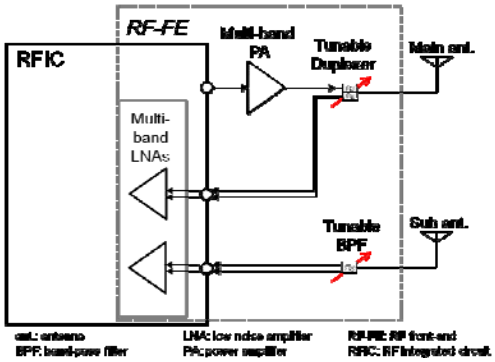

Fig.2. Block diagram example of RF front-end employing multi-band and/or tunable RF circuits

Fig. 2 shows a single-path configuration of multi-band RF-FE which employs the reconfigurable or tunable PA and filters. For the PA, we have proposed use of single-band devices with distributed reconfigurable matching networks [4-6]. Considering the difficulties in configuring a practical tunable band-pass filter as a top filter or

duplexer, collaboration between the filter and LNA is a candidate to achieve the performance level required for the RF-FE [7]. This paper overviews the recent progress in our research on the multi-band PA and LNA.

2. Multi-band PA

A PA is one of the key components in the RF-FE because its power consumption affects operating time of the mobile terminal. Conventional configuration of RF-FE shown in Fig. 1 employs single-band PAs or narrow-band PAs that are optimized for a specific frequency band and modulation scheme (mode) operation. In a PA design, there are trade-off relationship between efficiency and frequency range. A PA based on broadband matching technique (wide-band PA) can cover closely-located frequency bands, such as 800, 850 and 900 MHz bands, in compensation for some efficiency degradation from the single-band PA. A wide-band PA is becoming popular because it can merge several PAs which should be required for the conventional RF-FE in a multi-band terminal. However, the wide-band PA is not practical to merge the PAs for widely spread frequency bands. On the other hand, a PA with reconfigurable or tunable matching network (MN) is expected to achieve high efficiency at each frequency band even if the bands are widely spread. The PAs have variable devices such as switches in their matching networks to change their operating frequency. Fig. 3 shows a basic circuit diagram of our proposed reconfigurable amplifier [4-6]. The amplifier is designed based on a single-stub tuning scheme so that the circuit topology is simple. The status of switches is set to optimized values for high efficiency based on narrow-band matching at each target frequency.

Fig. 4 shows the block diagram of the reconfigurable 3-stage multi-band PA prototype [6], which covers the various frequency-bands between 1.5 GHz and 2.5 GHz. The input MN of the first stage (MN1) and the MN between the first and second stage (MN2) are designed to have broadband matching characteristics without switches. The reconfigurable MNs, called band-switchable MNs, are used in the MN between the second and third stage (MN3) and the output MN of the third stage (MN 4). Fig. 5 is a photograph of the PA prototype on a 4-layered printed-circuit board (PCB) sized as 6.2 x 8.05 mm^2. Three GaAs heterojunction bipolar transistors (HBTs) at each stage are integrated into one chip, which downsizes the PA remarkably. The PA also employs InGaAs pseudomorphic high electron mobility transistor switches in the band-switchable MNs. In total, 12 switches are used in the PA, and they are integrated into 5 dies, as “Sw” in Fig. 5. The MNs also use surface mount type chip capacitors. The bias feed lines of the switches are assigned to the intermediate layers of the PCB. These points also aid in compacting the PA. Fig. 6 shows the frequency responses for 5 operation modes, i.e., the 1.5-GHz mode, 1.7-GHz mode, 1.8/1.9-GHz mode, 2.3-GHz mode, and 2.5-GHz mode. The gain exceeds 25.5 dB at the targeted frequency range in each operation mode. The input and output reflection characteristics are approximately -10 dB and -6 dB in all frequency bands. The detailed characteristics of the PA are shown in [6].

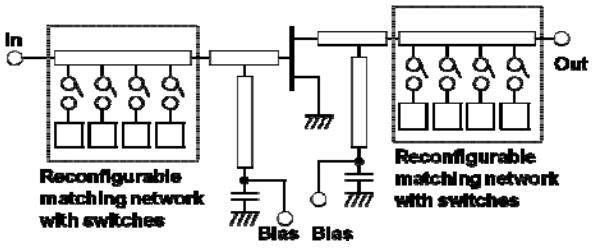

Fig.3. Basic configuration of the proposed reconfigurable PA

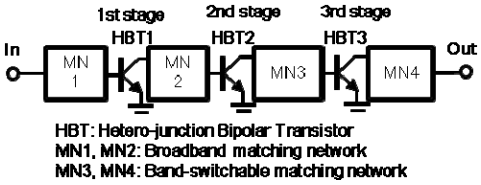

Fig.4. Block diagram of the 3-stage PA

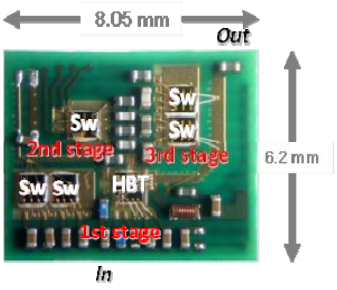

Fig.5. Photograph of the 3-stage PA[6]

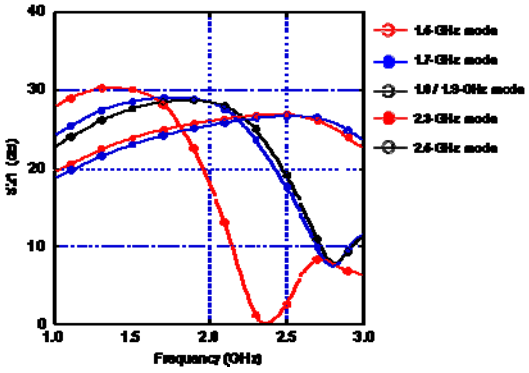

Fig.6. Frequency response of the 3-stage PA[6]

3. Multi-band LNA

It is a considerable challenge to attain a tunable BPF with low-loss and a wide-tuning frequency range. Considering a tunable BPF as a part of duplexer, one of the serious problems for receivers is to generate gain and phase modulation caused by strong out-of-band signals, such as transmitted signals in other frequency band. The LNA will be

required to enhance its frequency selectivity in order to prevent the performance degradation from undesired out-of-band signals in a multi-band receiver that yields non-optimum RF filter performance. Collaboration between the filter and LNA is a candidate to achieve the performance level required for the RF-FE. To investigate the collaboration, the frequency response adjustment of the LNA will be a solution.

Fig. 7 shows a photograph of the reconfigurable amplifier, which has a similar circuit topology shown in Fig. 3 [7]. The amplifier consists of a GaAs Field Effect Transistor (FET), input and output MNs with switches, and biasing networks with a high-impedance transmission line. Each MN has transmission lines, shorted or open stubs, and four MEMS switches. All the chips and chip capacitors for biasing circuits are mounted on a 19 x 13 mm^2 PCB. Fig. 8 shows small signal frequency responses of the amplifier in two switch states (0 for broadband and 1 for narrow-band) at a class A bias condition. Different frequency responses are obtained through the switch status control. From the results of the gain suppression measurement at 3.1 GHz with out-of-band signals of 2 GHz, the gain suppression is observed at a higher level of out-of-band signal input power, and is mitigated in the narrow-band configuration [7]. The reason considered for this is that the gain degradation at 2 GHz occurs at a lower input level in the broadband configuration because of the high gain at out-of-band signal frequency. Thus, the proposed reconfigurable amplifier is effective in the gain suppression problem caused by out-of-band signals.

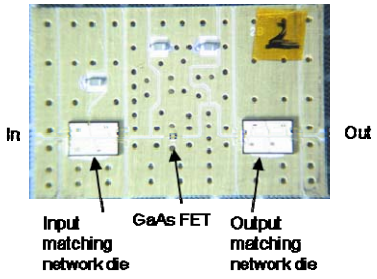

Fig.7. Photograph of the reconfigurable amplifier

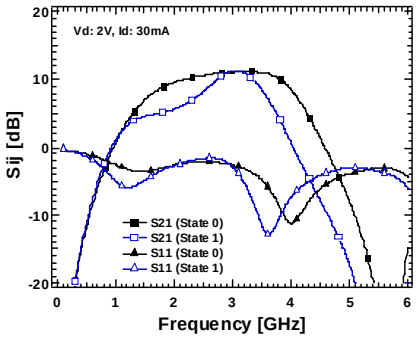

Fig.8. Frequency responses of the reconfigurable amplifier

4. Conclusion

This paper introduced recent results on our reconfigurable PA and LNA. Even though there are still some issues to be solved to achieve reconfigurable RF front-end for future mobile terminals, such as efficiency improvements of PA and detailed studies on collaboration between filters and LNA, we believe these RF circuits will contribute to the multi-mode band-free operation in future mobile terminals with further studies.

References

1. A. Moris, “MEMS-based Tuning for RF Front-ends,” in IEEE MTT-S International Microwave Symposium 2013 Workshops, WSJ-3, June 2013.
2. G. Hueber, R.B. Staszewski, Eds., Multi-Mode/Multi-Band RF Transceivers for Wireless Communications: Advanced Techniques, Architectures, and Trends, John Wiley & Sons, Inc. Hoboken, New Jersey, 2011.
3. A. Bezooijen, R. Mahmouji,A. Roermund, Adaptive RF Front-Ends for Hand-held Applications, Springer, Dordrecht/Heidelberg/London/New York, 2011.
4. A. Fukuda, H. Okazaki, T. Hirota, and Y. Yamao, “Novel 900 MHz/1.9 GHz dual-mode power amplifier employing MEMS switches for optimum matching,” IEEE Microwave and Wireless Components Letters, Vol. 14, pp. 121–123, March 2004.
5. H. Okazaki, A. Fukuda, K. Kawai, T. Furuta, and S. Narahashi, “MEMS-based Reconfigurable RF Front-end Architecture for Future Band-free Mobile Terminals,” in Proc. 37th European Microwave Conf., pp. 1058–1061, Oct. 2007.
6. T. Furuta, A. Fukuda, K. Kawai, H. Okazaki, and S. Narahashi, “Compact 1.5 GHz to 2.5 GHz multi-band, multi-mode power amplifier,” IEICE Electronics Express, Vol. 8, No. 11, pp. 854-858, June 2011.
7. H. Okazaki, K. Kawai, A. Fukuda, T. Furuta, and S. Narahashi, “Reconfigurable Amplifier Towards Enhanced Selectivity of Future Multi-band Mobile Terminals,” in IEEE Int. Microwave Workshop Series on RF Front-ends for Software Defined and Cognitive Radio Solutions, pp. 13–16, Feb. 2010.

Man-Made Noise Evaluation for Cryogenic Receiver Front-End

Shoichi Narahashi, Kei Satoh, and Yasunori Suzuki

Research Laboratories, NTT DOCOMO, INC., 3-6 Hikari-no-oka, Yokosuka, Kanagawa 239-8536 Japan
{narahashi,satokei,suzukiyasu}@nttdocomo.co.jp

Abstract. This paper introduces measured results of man-made noise impact on an cryogenic receiver front-end (CRFE) in urban and suburban areas in the 2-GHz band with amplitude probability distribution (APD). The CRFE, comprising a high-temperature superconducting filter, cryogenically-cooled low-noise amplifier, and highly-reliable cryostat, is expected to be an effective and practical approach to attain efficient frequency utilization and to improve the sensitivity of mobile base station receivers. It is important to measure the characteristics of man-made noise in typical cellular base station antenna environments and confirm their impact on the CRFE reception with APD because if man-made noise has a stronger effect than thermal noise, the CRFE would fail to offer any improvement in sensitivity. Measured results suggest that the contribution of man-made noise in the 2-GHz band can be ignored as far as Wideband Code Division Multiple Access (W-CDMA) system is concerned. The man-made noise is also measured in the VHF-band for comparison with the 2-GHz band environment.

1. Introduction

A cryogenic receiver front-end (CRFE), comprising a high-temperature superconducting filter (HTSF), a cryogenic low-noise amplifier (CLNA), and a highly reliable compact-sized cryostat, is anticipated to be an effective and practical way to achieve efficient frequency utilization and high sensitivity performance for mobile base station receivers [1]-[3]. This is because the HTSF achieves low insertion loss and sharp skirt characteristics. High frequency selectivity characteristics can also reduce the saturation power level required for the cryogenic low-noise amplifier used in the base stations since undesired interference signals in the adjacent passband can be thoroughly suppressed resulting in mitigation of the cryostat cooling capability. In this paper, sensitivity represents the minimum received signal power level required to establish successfully a radio communication link between the mobile station and base station.

Two types of practical antenna noise characteristics for base station receivers are considered to investigate the effect of employing the CRFE. One is the equivalent noise temperature [4], which is an index for evaluating the thermal noise. The equivalent noise temperature represents the average power of the antenna noise at the input port of the base station receiver [2]. The other characteristic is derived from the amplitude probability distribution (APD) method [5], which provides amplitude distribution analysis data for the antenna noise envelope. This is useful in estimating the impact of man-made noise such as impulsive noise, lightning pulses, or interference on the received signals. There were reports on measurement results of impulsive noise pertaining to the electromagnetic environment for the universal mobile telecommunication system (UMTS) by using a normal temperature receiver front-end (RFE) comprising a bandpass filter and low-noise amplifier [6].

This paper introduces the measured results of man-made noise in urban and suburban areas for the 2-GHz band by applying the APD method [7]. The measured results show that the influence of man-made noise can be ignored as far as the W-CDMA system is concerned. The man-made noise is also measured in the VHF-band for comparison with the 2-GHz band environment [7].

2. Measurement Systems

2.1. Cryogenic Receiver Front-End

Fig.1. Example of tower-mounted RFE

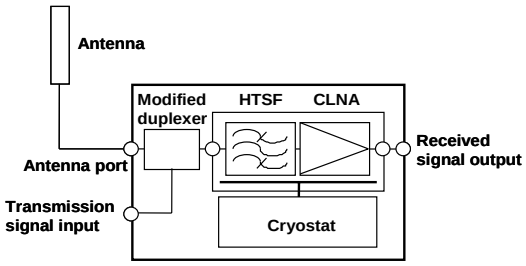

Fig.2. Fundamental CRFE configuration

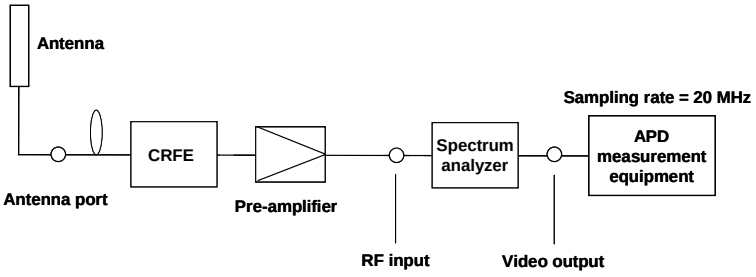

Fig. 3 Configuration of APD measurement

Figure 1 shows an example of an existing tower-mounted RFE. In base station receiver systems, the CRFE mounted on top of the tower appears to be the most promising approach to maximize the sensitivity and efficiency of the frequency utilization. Figure 2 shows the fundamental CRFE configuration. In this figure, a modified duplexer is inserted in front of the HTSF. The CRFE should be lightweight, small, and highly reliable to offer easy installation and maintenance because it is to be installed near the top of the tower, similar to the conventional RFE.

2.2. Measurement System

Figure 3 shows the configuration of the APD measurement experiment. The target noise is measured at center frequency f_c of the spectrum analyzer in the zero-span mode. The intermediate frequency (IF) bandwidth, which corresponds to the resolution bandwidth (RBW) of the spectrum analyzer, must be set sufficiently wide when evaluating the instantaneous value of noise because it is difficult to observe the influence of the man-made noise if the IF bandwidth is too narrow. In other words, it is ideal to measure noise with the IF bandwidth of a specific signal when evaluating the influence of noise on that specific signal. Thus, the noise waveform observed for specific frequency f_c is derived from the video output port of the spectrum analyzer. Reference [7] shows the details of the measurement system.

3. Measurement Results

3.1. 2-GHz Band Experiment

In this experiment, center frequency f_c of the spectrum analyzer in Fig. 3 is set to 1.949 GHz after spectrum observation of the passband width of the CRFE to avoid specific frequencies that may be used by other communication systems. The antenna in Fig. 3 is a co-linear array antenna that has a 60-degree beamwidth in the horizontal plane and a 5-degree beamwidth in the vertical plane, as shown in Fig. 4.

Zero- and six-degree beam tilt angles are used for the measurement. The measuring time interval is 1 h in the evening for each beam tilt angle. The antenna height is approximately 70 m in the suburban area, and approximately 100 m in the urban area. The IF bandwidth is set to 1 MHz because the upper limit of the spectrum analyzer used in this experiment is 1 MHz, although the IF bandwidth of the W-CDMA system is 3.84 MHz [8].

Figure 5 shows some typical APD data for the 2-GHz band in the urban and suburban areas. In the figure, the APD, which was measured by connecting a 290 K terminator to the input port of the CRFE, is also plotted in order to determine the thermal noise level. The reference point of the abscissa in Fig. 5 is the minimum value of the noise envelope derived by connecting the 290 K terminator. The APD data for the antenna noise almost coincide with those of the thermal noise at probabilities higher than 10^{-4}. Here, the following three assumptions are employed to conduct a rough but fundamental estimation of the influence of the received noise on the W-CDMA system: (1) Thermal noise is dominant above while man-made noise is

dominant below the probability of 10^{-4}. (2) The APD value is an indicator of the bit error rate (BER) measured in front of the detector. This is because instantaneous bit error might be caused when the instantaneous noise power exceeds the threshold level signifying error. (3) Although the IF bandwidth for the W-CDMA system is 3.84 MHz, the difference between 3.84 MHz and 1 MHz (used in this experiment) is inconsequential with regard to the APD characteristics.

Fig.4. Example of experimental environment in 2-GHz band

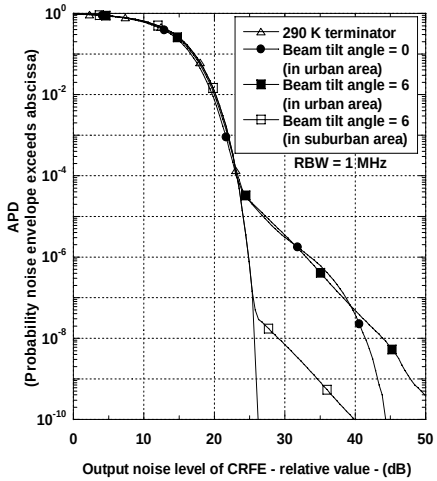

Fig.5. APD of antenna noise in 2-GHz band

From Fig.5, the major noise at the corresponding amplitude probability distribution of 10^{-3} is only thermal noise since the W-CDMA system employs very strong error correction techniques and therefore requires a minimum BER of approximately 10^{-3} for both voice and data. This suggests that the contribution of man-made noise can be ignored as far as the W-CDMA system is concerned and sensitivity improvement offered by the CRFE will be attained.

3.2. VHF-Band Experiment

The man-made noise is also measured in the VHF-band for comparison with the 2-GHz band environment in a similar manner as the 2-GHz band experiment. However, there are some differences in the measuring configuration: (1) The RFE is used instead of the CRFE. (2) Center frequency f_c of the spectrum analyzer is set to 264 MHz. (3) The RBW of the spectrum analyzer (IF bandwidth) is set to 30 kHz. (4) A double ridged guide antenna is used, as shown in Fig. 6. (5) The antenna height is approximately 50 m in the suburban area, and approximately 95 m in the urban area.

Figure 7 shows typical APD data for the VHF-band in the urban and suburban areas. The APD data exhibit a definite difference compared to those in the 2-GHz band. In the urban area, a 3-dB or higher noise level is observed below the probability of 0.1 compared to the case for the thermal noise. Impulsive noise can be observed around the probability of 10^{-2} and 10^{-4}, respectively. In the suburban area, the difference from the thermal noise is apparent below the probability of 10^{-2} and impulsive noise can be observed around 10^{-3} and 10^{-5},

Fig.6. Example of experimental environment in 2-GHz band

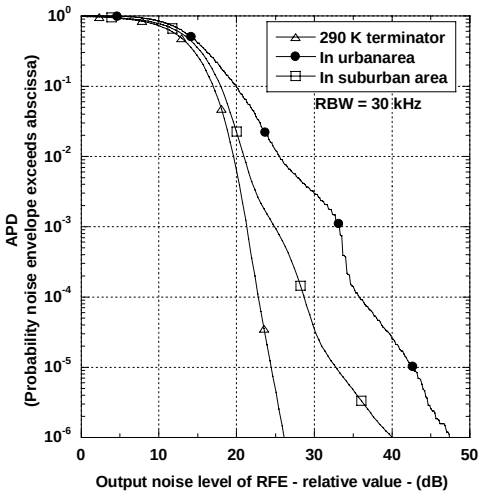

Fig.7. APD of antenna noise in 2-GHz band

respectively. In the VHF-band, a more detailed investigation is required to assess the sensitivity improvement based on the communication system requirements to which the CRFE is to be applied.

4. Conclusion

Man-made noise was evaluated in the 2-GHz band and VHF-band using the APD method in typical cellular base station antenna environments from the standpoint of improving the sensitivity by employing the CRFE. Experimental results show that the influence of man-made noise can be ignored as far as the W-CDMA system is concerned. There is still need for discussion on the applicability of the CRFE to the VHF-band in detail. Measuring man-made noise in long time intervals for seasonal factor analysis is left for future investigation.

References

1. A. I. Braginski, “Superconducting electronics coming to market,” IEEE Trans. Appl. Supercond., vol. 9, no. 2, pp. 2825-2836, June 1999.
2. T. Nojima, S. Narahashi, T. Mimura, K. Satoh, and Y. Suzuki, “2-GHz band cryogenic receiver front end for mobile communication base station systems,” IEICE Trans. Commun., vol. E83-B, no. 8, pp. 1834-1843, Aug. 2000.
3. S. Narahashi, K. Satoh, K. Kawai, D. Koizumi, and T. Nojima, “Cryogenic receiver front-end with sharp skirt characteristics,” Supercond. Sci. Technol., no. 19, pp. S416-S422, 2006.
4. H. Taub and D. L. Schilling, Principles of Communication Systems. 2nd edition, pp. 621-626, McGraw-Hill, New York, 1986.
5. M. Uchino, Y. Hayashi, T. Shinozuka, and R. Sato, “Development of low-cost high-resolution APD measuring equipment,” 1997 International Symposium on Electromagnetic Compatibility Proceedings, pp. 253-256, Beijing, China, May 1997.
6. M. G. Sanchez, A. V. Alejos, and I. Cuinas, “Urban wide-band measurement of the UMTS electromagnetic environment,” IEEE Trans. Veh. Tech., vol. 54, no. 4, pp. 1014-1022, July 2004.
7. S. Narahashi, K. Satoh, Y. Suzuki, T. Mimura, and T. Nojima, “Man-Made Noise Evaluation for Cryogenic Receiver Front-End,” Journal of Communications, vol. 3, No.5, pp. 54-61, October 2008.
8. 3GPP, Technical Specification TS 25.101, http://www.3gpp.org, 1999.

Implementation of Digital Signal Processors in Control Systems

Petko Petkov and Tsonyo Slavov

Department of Systems and Control, Technical University of Sofia,
8 Kliment Ohridski Str., 1000 Sofia, Bulgaria,
{php, ts_slavov}@tu-sofia.bg

Abstract. Digital Signal Processor (DSP) implementation of H_∞ and μ-controllers for real-time robust control of a multivariable system is presented. An 8th order discrete-time H_∞-controller and a 16th order μ-controller are implemented with sampling frequency of 100 Hz by using Texas Instruments TMS320F28335 Digital Signal Processor. An appropriate software in MATLAB™/Simulink™ environment is developed which is embedded in DSP by using the Simulink Coder™. Experimental and simulation results are presented which confirm that both control systems achieve the prescribed performance.

1. Introduction

The Robust Control Theory involves powerful methods for analysis and design of control systems in presence of signal and parameter uncertainties. In contrast with the theoretical achievements, the practical implementation of robust control laws is still in its beginning. The main obstacle of robust control laws implementation is the difficulties related to the development, testing and verification of the necessary real-time software. These difficulties are reduced significantly using the recent technologies for automatic code generation and embedding implemented in MATLAB™/Simulink™ program environment.

In this paper we present the implementation of H_∞ and μ-controllers for real-time robust control of multivariable 4th order two input/two output laboratory plant. An 8th order H_∞ controller and a 16th order discrete-time μ-controller with sampling frequency of 100 Hz are implemented by using the Texas Instruments TMS320F28335

Digital Signal Processor (DSP). An appropriate software in MATLAB™/ Simulink™ environment is developed which is embedded in DSP by using the Simulink Coder™. Experimental and simulation results are presented which confirm that both control system achieve the prescribed performance.

2. DSP Implementation for Robust Real-Time Control

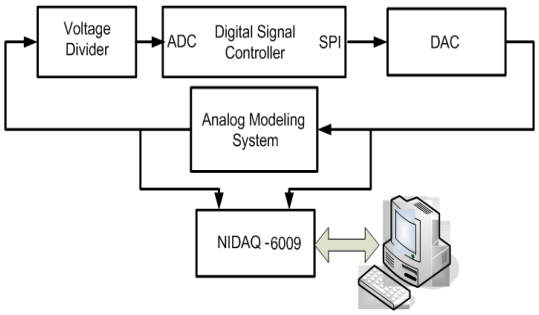

Fig.1. Block-diagram of the control system with DSP

The block-diagram of developed control system with DSP is shown in Fig. 1. The block ``Digital Signal Controller'' (DSC) is the Spectrum Digital eZdspTMF28335 development board with an integrated Digital Signal Processor Texas Instruments TMS320F28335 [1]. This controller works at 150 MHz and may perform single precision (32-bit) computations by using Floating-Point Unit (FPU). It has 68K bytes on-chip RAM, 256K bytes off-chip SRAM memory, 512K bytes on-chip Flash memory and on-chip 12 bit Analog to Digital (A/D) converter with 16 input channels. The two input/two output plant is modeled on an analog modeling board, consisting of a bus on which functional blocks are operating independently. The bus is powered by a DC power supply. The linear range of input-output signals is ±10 V. The main linear blocks are adder, differentiator, inverter, integrator, aperiodic unit and gain unit. The analog system makes it easy to model plants with a time constant up to 1s and gain factor up to 10. The block ``Voltage Divider'' is a specially designed dual channel board, which converts linearly two input analog signals with range -5 ÷ 5 V into two analog output signals with range 0 ÷ 3 V. The block ``DAC'' is a digital to analogue converter DAC8734EVM produced by Texas Instruments [2]. The DAC is 16-bit, quad-channel and can be configured to outputs ±10V, ±5V, 0V to 20V or 0V to 10V. It features a standard high-speed serial peripheral interface (SPI) that operates at clock rates of up to 50 MHz to communicate with a DSP. The block ``NIDAQ-6009'' is a specialized module for data acquisition NIDAQ-6009 of National Instruments [3]. Specially developed software provides the user interface, connection and exchange input/output data with a standard PC in real time.

The control algorithm is embedded and runs with frequency 100 Hz on the DSC. The software development environment includes MATLAB™ v. 7.11.0.584 (R2010b), Simulink™ v. 7.6, Simulink Coder™ v. 7.6 [4], Embedded Coder™ v. 5.6 [5], Microsoft Visual C++ v. 8.0 and Code Composer Studio™ (CCS) v. 3.3. A technology for automatic generation and embedding the code using the Simulink Coder™ is implemented. The main advantages of this technology are the relatively easy implementation of complex control algorithms and the short time to translate the control algorithm from the working simulation environment to the real working environment with physical plants, reducing the overall time for application testing and verification of the developed algorithm.

The H_∞ and μ-controllers are designed by the methods described in [6,7,8], implemented using DSP and tested experimentally. Further on we show the experimental transient responses of the closed-loop system for both controllers compared with the corresponding simulation results. The experiments are done for a zero reference and a sinusoidal disturbance with magnitude 1 V and frequency 1 rad/s which is added to the first output of the system at the 5th second. In order to assess the influence of the processor precision the experiments are performed using single as well as double precision arithmetic.

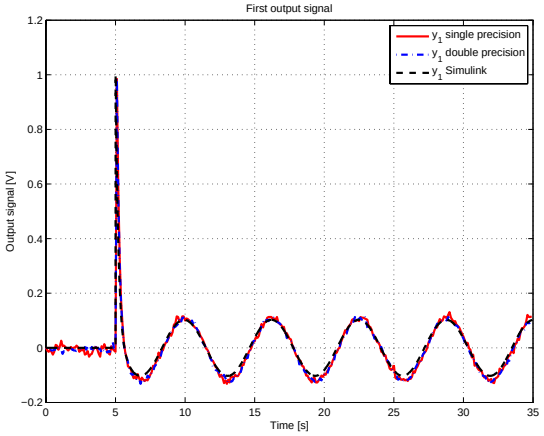

Fig.2. First output signal for H_∞ controller

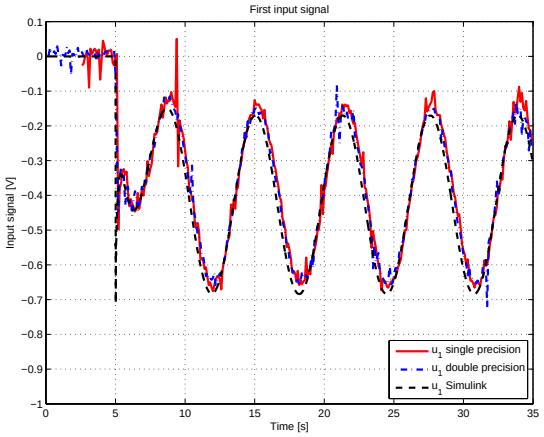

Fig.3. First control signal of H_∞ controller

The first output and control signals from experiments and simulation are shown in Fig. 2 and Fig. 3, respectively (here and further on all signals are measured in volts). After the initial deviation at the 5th second the first output quickly decreases and

oscillations with magnitude 0.12 V are settled, i.e., the disturbance is attenuated approximately 10 times. (Note that the steady-state oscillations around the equilibrium point of the second output are negligible.) The Figure displaying first control signal shows a good coincidence between experimental and simulation results. The plots show that the errors are slightly greater in the case of using single precision arithmetic.

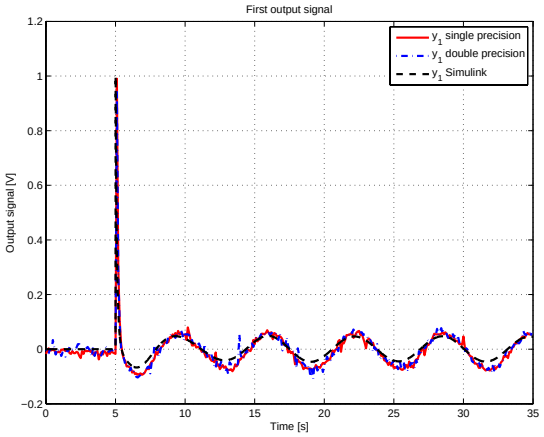

Fig.4. First output signal for μ-controller

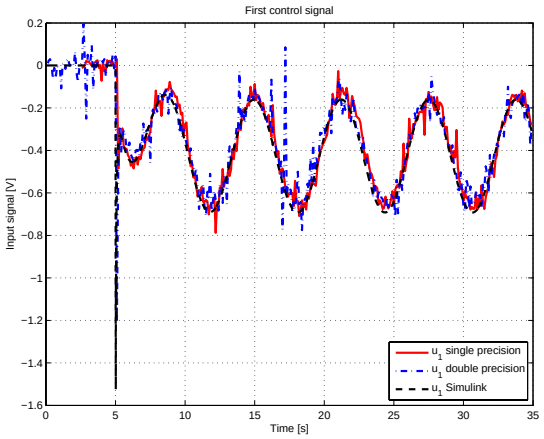

Fig.5. First control signal of μ-controller

The first output and control signals from simulation and experiments for the case of μ-controller are shown in Fig.4 and Fig.5, respectively. It may be observed that the magnitude of the steady-state error in the output is smaller than the error in case of H_∞ controller. As in the case of H_∞ controller, the plots of control signals show the presence of some small deviations from simulation results. This is explained by the

properties of the corresponding transfer function matrix which amplifies the noises in the control signals.

3. Conclusion

It should be noted that the hardware and software developed may be used with minor changes in the control of other multivariable systems provided the appropriate controllers are designed.

References

1. Spectrum Digital, Inc. eZdspTMF28335 Technical Reference, 2007. Available from: http://c2000.spectrumdigital.com/ezf28335/docs/ezdspf28335c_techref.pdf
2. Texas Instruments. DAC8734 Evaluation Module, 2009. Available from: http://www.ti.com/tool/dac8734evm
3. National Instruments. NI USB-6009 14-Bit, 48 kS/s Low-Cost Multifunction DAQ. Available from: http://sine.ni.com/nips/cds/view/p/lang/en/nid/201987
4. The MathWorks, Inc. Simulink Coder™ User's Guide. Natick, MA, 2011. Available from: http://www.mathworks.com
5. The MathWorks, Inc. Embedded Coder™. Natick, MA, 2011. Available from: http://www.mathworks.com
6. K. Zhou, J.C. Doyle, K. Glover. Robust and Optimal Control. Prentice Hall, Upper Saddle River, NJ, 1996.
7. D.-W. Gu, P.H. Petkov, M.M. Konstantinov. Robust Control Design with MATLAB™, 2nd ed. Springer-Verlag, London, 2013.
8. G. Balas, R. Chiang, A. Packard, M. Safonov. Robust Control Toolbox User's Guide, The MathWorks, Inc., Natick, MA, 2013. Available from http://www.mathworks.com/help/pdf_doc/robust/robust_ug.pdf

Speech Signals Quality Assessment in the Cellular GSM Network

Damyan Damyanov

Technical University of Sofia, Faculty of Automation, Department for Industrial Automation,
Darvenitsa 1756, Bul. Kliment Ohridski 8, Bulgaria
damyan_damyanov@tu-sofia.bg

Abstract. The great success of the GSM - network is not only due to technical factors. The GSM-Standard was developed by ETSI as an open standard, and allows competition between providers of telecommunication services. When assessing the quality of speech signals at the end user, all parameters, that are available in practice, are more or less indicators for the performance of the GSM network. When using the GSM - network "anywhere, anytime" it is actually necessary to introduce objective criteria for the speech signal quality assessment. This paper introduces a new system for the accomplishing of this task.

1. Introduction

For the quality assessment of the speech signals in the GMS - network two communication modules are used.

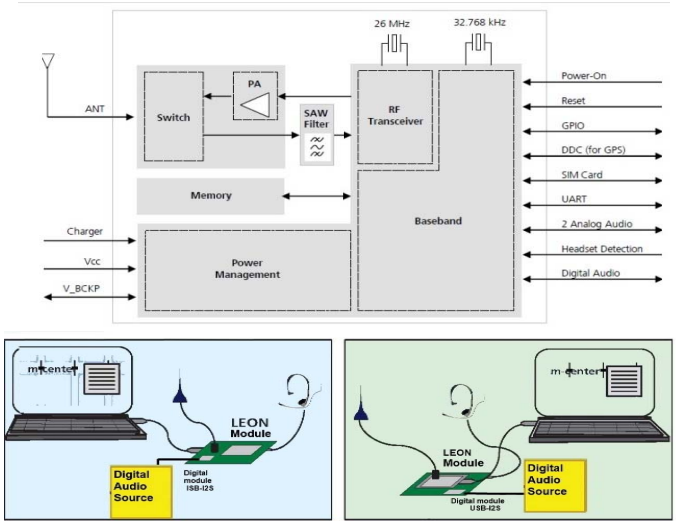

Fig.1. Architecture of the module LEON G200 GSM Block diagram of the developed stand

These are of type LEON - G200 GSM. They have a built-in GSM protocol. For the purpose of the experiments a digital module type USB-I2S is used, which transmit digital audio to the LEON module. The architecture of the module LEON G200 GSM and the wiring between the LEON Module, the digital USB-I2S module and the PC is given schematically in fig. 1.

2. Experimental Setup

The quality of the communication between two subscribers of one mobile operator has been tested. The SIM modules of this operator were placed in each LEON-Module, in order to make a connection in the GSM-Network.

As source of digital audio, the sound cards of the PC's, shown in fig 1 are used. As test signals, pseudo-phonetic sequences generated by the author are used. The time-frequency analysis of the speech signals in the receiver and transmitter is done with the help of the program MAGIX Audio Cleaning Lab Deluxe, paid license.

In order to visualize the results from the experiments, the following example is given:

The test signal in digital form at the transmitter has the following characteristics:

- Segment length 2.5 sec,
- Sampling frequency 44100 Hz
- Pitch - 120 Hz
- No noise nor attenuation is been added to the segment
- 7 formants with the following characteristics
    - First formant - frequency 240 Hz, amplitude 0.75 , initial phase 0 rad
    - Second formant - frequency 360 Hz, amplitude 0.15 , initial phase 0 rad
    - Third formant - frequency 480 Hz, amplitude 0.25 , initial phase 0 rad
    - Fourth formant - frequency 600 Hz, amplitude 0.32 , initial phase 0 rad
    - Fifth formant - frequency 720 Hz, amplitude 0.40 , initial phase 0 rad
    - Sixth formant - frequency 840 Hz, amplitude 0.20 , initial phase 0 rad
    - Seventh formant - frequency 960 Hz, amplitude 0.20 , initial phase 0 rad

The waveform of the signal and the spectrum of the transmitted test signal is shown in fig 2:

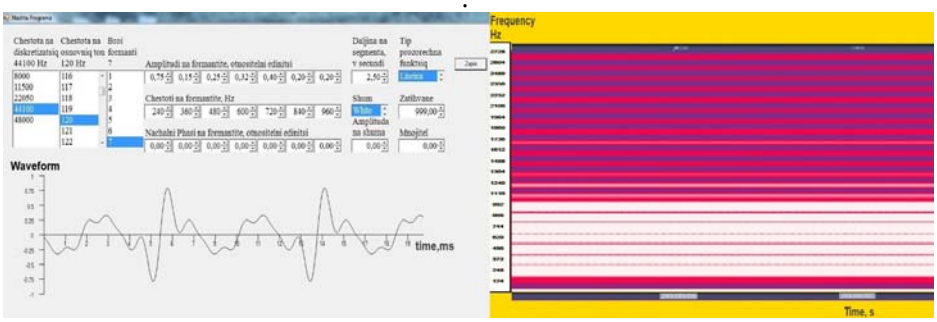

Fig.2. Waveform and Spectra of the generated test signal

This signal contains all the features of the letter "a", pronounced by a Bulgarian male. After the generation and the recording of the test signal on the first PC, a connection with the digital module and the LEON module has been made. Then, using the software called m-center, contained in the package of the LEON modules, a connection between the two LEON modules over the GSM-Network has been established. A photographic image of the stand and a snapshot of the work of the program m-center is shown in fig 3:

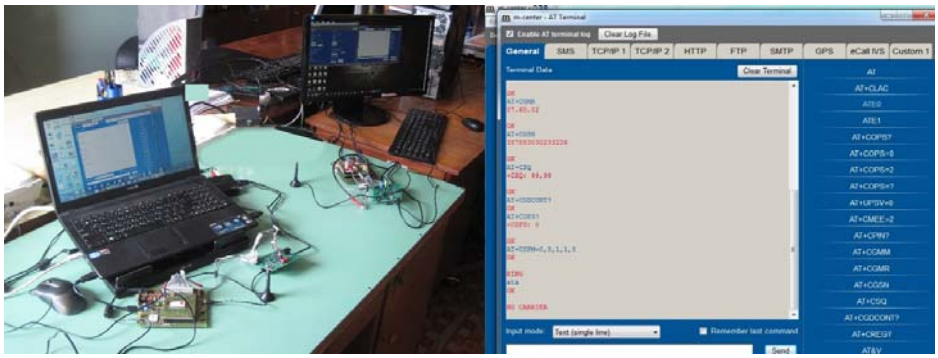

Fig.3. A photo of the stand and a snapshot of the work of the program m-center, showing the connection between the two LEON modules over the GSM- Network

Through the USB port of the first computer, the test signal in digital form is sent to the digital module USB-I2S. The digital module sends the digital signal to the LEON module. The LEON module transmits the digital to the second module over the GSM-Network. The second LEON module receives the signal in digital form, converts it in analog form and sends it to the sound card of the second PC. Then, in the second PC, the signal is digitized and recorded. The waveform and spectra of the received signal are shown in fig 4:

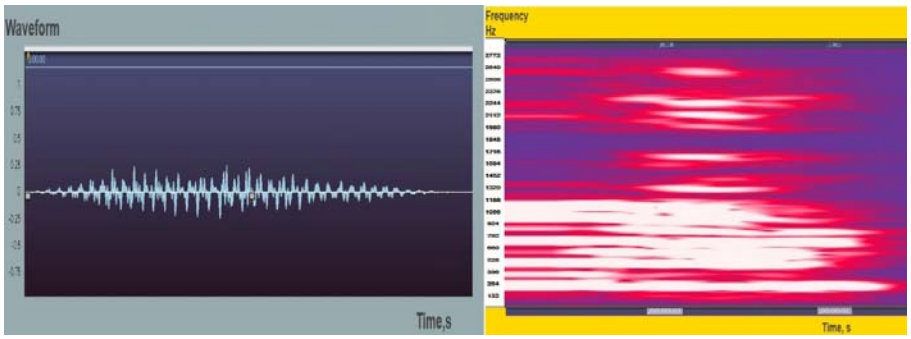

Fig.4. Wave form and Spectra of the received test signal

The received signal, carried over the GSM network of the mobile operator has the following features:

- Segment length 2.5 sec,
- Pitch - due to the characteristics of the GSM - Network, the pitch is not transmitted
- 7 formants with the following characteristics
  - First formant: frequency 240 Hz, amplitude 1.00 , initial phase $0.12\,\pi\,rad$
  - Second formant: frequency 480 Hz, amplitude 0.49 , initial phase $0.10\,\pi\,rad$
  - Third formant: frequency 600 Hz, amplitude 0.35 , initial phase $0.09\,\pi\,rad$
  - Fourth formant: frequency 720 Hz, amplitude 0.37 , initial phase $0.07\,\pi\,rad$
  - Fifth formant: frequency 840 Hz, amplitude 0.12 , initial phase $0.09\,\pi\,rad$
  - Sixth formant: frequency 960 Hz, amplitude 0.25 , initial phase $0.12\,\pi\,rad$
  - Seventh formant: frequency 1080 Hz, amplitude 0.22 , initial phase $0.10\,\pi\,rad$

3. Proposed system for speech signal quality assessment in the GSM-Network

The index, which facilitates the interpretation of each one the indicators of the quality of the speech signal, transmitted over the GSM-Network, and the connection between each two of the indexes, is their correlation [1, 2]. For example, the BER can be used for measuring the speech quality, but in order to analyze the voice quality, it is necessary to introduce the correlation between the BER and the speech quality [3, 4]. This correlation is not constant, it depends on the profit from the decoding, which is dependent on the channel encoding and the channel profile. Furthermore, the mobile networks of the second generation, using circuit switching for the transmission of voice signals, use very narrow spectral band for each channel [5, 6]. The open standard of ETSI has a set of recommendations for the measurement and evaluation of the quality of service, but at present no unified standard for assessing the speech quality of signals, transmitted over the GSM-Network is available. However, in theory and practice, a huge number of objective and subjective methods for measuring and assessing the quality of speech signals, transmitted over different networks, including the GSM network, are present [1, 2, 7].

The developed laboratory stand allows the implementation of a universal system for assessing the quality of speech signals in the GSM-Networks. When speech signals are transmitted over the GSM - network, non-linear distortion occurs, the most important parts of which are:

- Deletion of formants in the spectrum of the speech signal,

- Appearing of spurious formants in the spectra of the received signal, not present in the original signal.

In addition to the non-linear distortion, changes in the amplitude and the initial phase of the formats occur.

These effects occur always, when speech signals are transmitted over the GSM-Network. Keeping that in mind, unambiguous criteria for assessing the quality of the voice service in the GSM-Network can be defined, namely:

- Gain of each formant of the spectrum of the signal:

  K_{A_i}

- Phase shift in the frequency of each formant of the signal:

  $K_{\varphi_i}\lfloor rad \rfloor$

- Number of added formants to the spectra of the signal

  $SPURF$

- Ratio of the biggest formant gain to the smallest nonzero gain:

  $$R_A = \frac{K_{A\max}}{K_{A\min}}$$

- Difference between the largest and smallest phase shift of the formants:

  $$R_\varphi = K_{\varphi\max} - K_{\varphi\min} \lfloor rad \rfloor$$

For the current example, these coefficients are as follows:

- Gain of each formant of the spectrum of the signal:

  $K_{A_1} = 1.33 \quad K_{A_2} = 0 \quad K_{A_3} = 1.96$
  $K_{A_4} = 1.09 \quad K_{A_5} = 0.93 \quad K_{A_6} = 0.6$
  $K_{A_7} = 1.25$

- Phase shift in the frequency of each formant of the signal:

  $K_{\varphi_1} = 0.12\pi\ rad \quad K_{\varphi_2} = 0{,}1\pi\ rad \quad K_{\varphi_3} = 0.09\pi\ rad$
  $K_{\varphi_4} = 0.07\pi\ rad \quad K_{\varphi_5} = 0.09\pi\ rad \quad K_{\varphi_6} = 0.1\pi\ rad$
  $K_{\varphi_7} = 0.12\pi\ rad$

- Number of added formants to the spectra of the signal

  $SPURF = 1$

- Ratio of the biggest formant gain to the smallest nonzero gain:

$$R_A = \frac{K_{A\max}}{K_{A\min}} = \frac{1.96}{0.6} = 3.3$$

- Difference between the largest and smallest phase shift of the formants:

$$R_\varphi = K_{\varphi\max} - K_{\varphi\min} = 0.12\pi - 0.07\pi = 0.05\pi \ rad$$

Conclusions

The most important degrees for the quality of the speech communication are broadcast quality, toll quality, communication quality, and synthetic quality [1]. With the introduction of the new voice codecs, which don't operate of the waveform of the signal, these degrees of speech signal quality are very vague at present. The quality of the analog network, which operates in terms of frequency responses and noise levels, was used to define the toll quality [1]. Since nowadays the analog networks are hardly used for industrial and civil purposes, it is difficult to define exactly this quality measure [2,3]. The proposed quality estimates in this paper pretend to be exactly defined and subjective.

References

1. John C. Bellamy, Digital Telephony John Wiley & Sons Inc, Chichester, UK. 1982.
2. Sivannarayana Nagireddi, VoIP Voice and Fax Signal Processing , 1st ed, John Wiley & Sons Inc, Hoboken, New Jersey, 2008.
3. Benesty B., Sondhi M.M., Huang Y., Springer Handbook of Speech Processing , Springer, Warren, New Jersey, 2008
4. ITU-T Rec. G711 Appendix I 1999. A High Quality Low-Complexity Algorithm for Packet Loss Concealment for G.711. Geneva: ITU Publication
5. ETSI EN 301 703 V7.0.2 1999-12. Adaptive Multi-Rate (AMR); Speech Processing Functions; General Description. (GSM 06.71 version 7.0.2, Release 1998) France: ETSI
6. Damyanov D., Galabov V., “Characteristics of the model of Fant of second order on speech production, ” Proceedings of Technical University - Sofia, vol. 62, Issue 2, pp. 181-188, ISSN 1311-0829, Sofia 2012
7. Damyanov D., Galabov V., “On the impact of duration of the phase of open glottis on the spectral characteristics of the phonation process, ” Proceedings of Technical University - Sofia, vol. 62, Issue 2, pp. 173-180, ISSN 1311-0829, Sofia 2012

Multiuser Coding for Gaussian Multiple-Access Channel

Jun Cheng and Guanghui Song

Dept. of Intelligent Information Eng. & Sci., Doshisha University, Kyoto 610-0321 Japan
jcheng@ieee.org and ghsong2008@hotmail.com

Abstract. Multiuser coding for Gaussian multiple-access channel is outlined. Two examples of multiuser coding: multiuser serial concatenated code and multiuser parallel concatenated code are given. The common feature of two multiuser codes is that each user employs a repetition code as its component code, which is powerful in mitigating user interference. For these multiple-access communication systems, an iterative multiuser detection and decoding is also described. Performance close to theoretical limits is observed by simulation and theoretical analysis.

1. Introduction

In a multiple-access channel (MAC), multiple users communicate with a single receiver over the common channel. Since there exist both user interference and channel noise, multiuser coding is necessary. To mitigate user interference, a traditional way of generating the user-specific codes is by employing distinct spreading codes, as in the well-known direct sequence CDMA (code-division multiple-access) [1] scheme. Another possibility is to distinguish between users using longer user-specific interleavers after spreading, as in IDMA (interleave-division multiple-access) schem [2] [3]. The longer interleaves may be regarded as rate-one codes.

On the other hand, to mitigate channel noise, each user in both CDMA and IDMA systems employing an error correction code (ECC). Since the spreading is in fact a repetition encoding, both the coded CDMA and coded IDMA can be regarded as multiuser serial concatenated codes (SCCs), where each user is a SCC with an outer ECC and an inner repetition code. Note that the inner repetition code has been shown as a powerful code for user separation [4].

It is nature to extend the idea of multiuser SCC to multiuser parallel concatenated code (PCC). Since the repetition code plays an important role in mitigating interference, each user's code should be a repetition code parallelly concatenated with an ECC.

In this paper, we outline multiuser coding for Gaussian multiple-access channel. We give two examples of multiuser coding: multiuser nonbinary SCC and multiuser PCC. The common feature of two multiuser codes is that each user employs a repetition code as its component code, which is powerful in mitigating user interference. For these multiple-access communication systems, an iterative multiuser detection and decoding is also described. Performance close to theoretical limits is observed by simulation and theoretical analysis.

2. Multiple-Access Communication System

A multiple-access communication system is shown in Fig. 1, where K users communicate with a common multiuser decoder over MAC. In the system, each user is assigned with code C^k with code rate R_k. For user k, information vector $\mathbf{u}^k = \left(u_1^k, ..., u_N^k\right)$, $u_i^k \in \{0,1\}$, is encoded based on code C^k into $\mathbf{x}^k = \left(x_1^k, ..., x_T^k\right)$, which is transmitted to the Gaussian MAC. Here the user encoder should be different for each user to make sure that the transmitted vector of each user is from a different vector set. For transmission, we will fovor $x_j^k \in \{+1,-1\}$ over $x_j^k \in \{0,1\}$ under mapping $\{0 \leftrightarrow +1, 1 \leftrightarrow -1\}$.

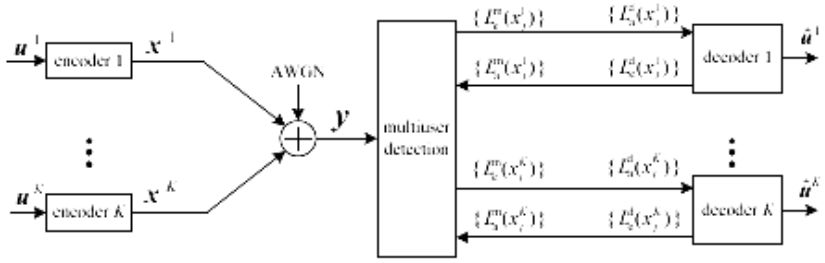

Fig. 1 *K*-user coding and decoding for multiple-access channel.

The receiver receives superimposed signal vector $\mathbf{y} = (y_1, y_2, ..., y_T)$ of K users with

$$y_j = \sum_{k=1}^{K} x_j^k + z_j, \quad j = 1,2,...,T \tag{1}$$

where $x_j^k \in \{+1,-1\}$ and z_j is a zero-mean Gaussian variable with a variance of σ^2. Multiuser decoding is to recover information vectors $\mathbf{u}^k$, $k = 1,\ldots,K$, from receive vector $\mathbf{y}$. The maximum *a posteriori* (MAP) decoding gives estimate $\hat{u}_j^k$ of original information bit u_j^k by

$$\hat{u}_j^k = \arg\max_{u_j^k \in \{0,1\}} \Pr\left(u_j^k \,|\mathbf{y}\right), \quad j = 1,2,...,T \tag{2}$$

2.1 Iterative Multiuser Detection and Decoding

We adopt an iterative receive, as shown in Fig.1, to approximately find MAP in Eq. (2). The iterative receive is carried out between a multiuser detection (e.g., an elementary signal estimation (ESE)) and K single-user *a posteriori* probability (APP) decoders. The multiple access and coding constraints are considered separately in ESE and decoders. The outputs of ESE and decoders are extrinsic log-likelihood ratios (LLRs) about x_j^k.

The multiuser detector, receive *a priori* LLRs about coded bits x_j^k sent from the decoder, defined as $L_a^m\left(x_j^k\right) \triangleq \log \dfrac{\Pr\left(x_j^k=+1\right)}{\Pr\left(x_j^k=-1\right)}$, which is initialized to 0 before the first iteration. Given *a priori* LLRs $\left\{L_a^m\left(x_j^k\right),\ \forall k,j\right\}$ for K users and channel observation $\mathbf{y}$, the goal of the multiuser detector is to compute extrinsic LLRs $L_e^m\left(x_j^k\right)$ about x_j^k.

$$\begin{aligned} L_a^m\left(x_j^k\right) &= \log \frac{\Pr\left(\mathbf{y}\middle| x_j^k=+1\right)}{\Pr\left(\mathbf{y}\middle| x_j^k=-1\right)} = \\ &= \log \frac{\Pr\left(x_j^k=+1\middle|\mathbf{y}\right)}{\Pr\left(x_j^k=-1\middle|\mathbf{y}\right)} - \log \frac{\Pr\left(x_j^k=+1\right)}{\Pr\left(x_j^k=-1\right)} \triangleq L^m\left(x_j^k\right) - L_a^m\left(x_j^k\right) \end{aligned} \tag{3}$$

where $L^m\left(x_j^k\right)$ is the *a posteriori* LLRs about x_j^k. Then the extrinsic LLRs are sent to K decoders.

Each of K decoders receives extrinsic LLRs $L_e^m\left(x_j^k\right)$ from the multiuser detector as channel LLRs $L_c^d\left(x_j^k\right)$. From the channel LLRs and according to the code constraints, the decoder computes *a posteriori* LLRs $L^d\left(x_j^k\right)$, which are improved LLRs about coded bits x_j^k. For detailed discussion of the decoding algorithm, see [5]. Channel LLRs $L_c^d\left(x_j^k\right)$ are subtracted from $L^d\left(x_j^k\right)$ to get exticnsic LLRs $L_e^d\left(x_j^k\right) \triangleq L^d\left(x_j^k\right) - L_c^d\left(x_j^k\right)$, which are sent to the multiuser detector as new *a priori* LLRs $L_a^m\left(x_j^k\right)$. The error performance can be improved by some iterations.

Finally, the decoder computes *a posteriori* LLRs $L^d\left(u_j^k\right)$ about information bits u_j^k. Taking its sign $\hat{u}_j^k = sign\left(L^d\left(u_j^k\right)\right)$ gives an estimation of information bit.

2.2 Detailed Descriptions of Multiuser Detection

Optimum detection in an MAC presents a complexity that is exponential with the number of transmitting users, *K*, and thus becomes infeasible for almost any multiuser scenario of practical interest. In [2], the use of an ESE is proposed. This detector performs a simple iterative soft interference cancellation of the symbols transmitted by the different users, based on the extrinsic information provided by the corresponding channel decoders.

Given *a priori* LLRs $\left\{L_a^m\left(x_j^k\right),\ \forall k, j\right\}$ and channel observation **y**, ESE is to approximately find extrinsic LLRs $\left\{L_e^m\left(x_j^k\right),\ \forall k, j\right\}$ in (3). First, we treat x_j^k as a random variable and use $L_a^m\left(x_j^k\right)$ to compute its mean and variance.

$$E\left[x_j^k\right] = (+1)\cdot \Pr\left(x_j^k = +1\right) + (-1)\cdot \Pr\left(x_j^k = -1\right) =$$
$$= \frac{\exp\left(L_a^m\left(x_j^k\right)\right) - 1}{\exp\left(L_a^m\left(x_j^k\right)\right) + 1} = \tanh\left(\frac{L_a^m\left(x_j^k\right)}{2}\right)$$

$$\mathbf{Var}\left[x_j^k\right] = \left(+1 - \mathbf{E}\left[x_j^k\right]\right)^2 \cdot \Pr\left(x_j^k = +1\right) + \left(-1 - \mathbf{E}\left[x_j^k\right]\right)\cdot \Pr\left(x_j^k = -1\right) = 1 - \mathbf{E}\left[x_j^k\right]^2$$

Second, we detect x_j^k by a Gaussian approximation of interference from the remaining users. We rewrite (1) as

$$y_j = x_j^k + \zeta_j^k \tag{4}$$

where $\zeta_j^l = \sum_{i=1, i\neq k}^{k} x_j^i + z_j$ represents a distortion term with respect to x_j^k. Using the central limit theorem, ζ_j^k in (4) can be approximated by a Gaussian random variable with

$$\mathbf{E}\left[\zeta_j^k\right] = \sum_{i=1,i\neq k}^{K} \mathbf{E}\left[x_j^k\right]$$

$$\mathbf{Var}\left[\zeta_j^k\right] = \sum_{i=1,i\neq ki}^{K} \mathbf{Var}\left[x_j^k\right] + \sigma^2$$

Since the direct computation of extrinsic LLR $L_e^m\left(x_j^k\right)$ in (3) is too complex, the following approximation is applied.

$$L_e^m\left(x_j^k\right) \approx \log\left(\frac{\Pr\left(y_i \middle| x_j^k = +1\right)}{\Pr\left(y_i \middle| x_j^k = -1\right)}\right) == \log\frac{\exp\left(-\frac{\left(y_i - E\left[\zeta_j^k - 1\right]\right)^2}{2Var\left[\zeta_j^k\right]}\right)}{\exp\left(-\frac{\left(y_i - \mathbf{E}\left[\zeta_j^k + 1\right]\right)^2}{2\mathbf{Var}\left[\zeta_j^k\right]}\right)} = \frac{2\left(y_i - \mathbf{E}\left[\zeta_j^k\right]\right)}{\mathbf{Var}\left[\zeta_j^k\right]} \tag{5}$$

Extrinsic LLR $\left\{L_e^m\left(x_j^k\right),\ \forall k, j\right\}$ will be as *a priori* LLRs input to K decoders. The iteration between the multiuser detector and K decoders, described in Section 2.1, gives an approximation of *a posteriori* $\Pr\left(u_j^k \middle| \mathbf{y}\right)$ in (2).

3. Two Multiuser Codes

Figure 1 depicts the general model of the multiple-access communication system, where user k's signal u^k is encoded by its user-specific ECC C^k. Generally speak, it is difficult to construct K user-specific ECCs when K is larger. For a practical implementation of multiuser coding, user k's code C^k maybe consists of the same ECC C for all users with a user-specific interleaver π^k followed, as in the conventional IDMA system [2]. Hence, user k will transmit the bitstream of $x^k = \pi^k(C(u^k))$ over the MAC. In this section, we give two examples of practical implementation of multiuser codes [6] [7].

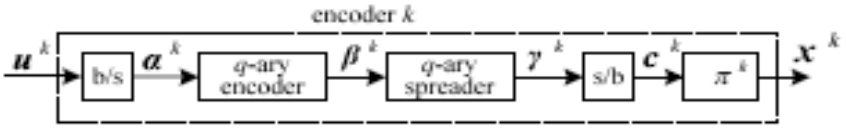

Fig. 2: User *k*'s encoder in multiuser SCC.

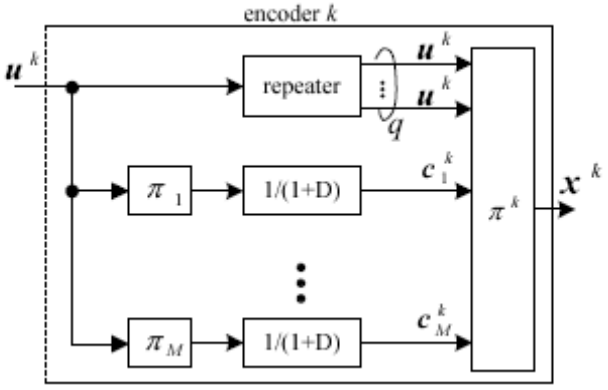

Fig. 3: User *k*'s encoder in multiuser PCC.

2.1 Multiuser Serial Concatenated Code

An implementation of multiuser code is a multiuser serial concatenated code (SCC). In fact, this is a coding-spreading IDMA system [2]. Figure 2 illustrates the user *k*'s encoder in multiuser SCC [6]. The encoder consists of a *nonbinary* ECC serially concatenated with a *nonbinary* spreading, and with user-specific interleaver π^k followed.

Let u^k be a binary information vector for user *k* with length *sN*. The binary vector is mapped into field symbol vector $\mathbf{a}^k = \left(a_1^k, ..., a_N^k\right)$, where $a_i^k \in \mathbf{GF}(q)$ with finite field **GF**(*q*), $q = 2^s$. This finite-field vector is encoded by a rate-R *q*-ary LDPC encoder, and the output codeword is denoted as $\beta^k = \left\{\beta_1^k, ..., \beta_n^k\right\}$, $n = \frac{N}{R}$, $\beta_i^k \in \mathbf{GF}(q)$. A *q*-ary spreading, which can be seen as a repetition coding, with length *L* is then performed on codeword β^k to generate field chip vector $\boldsymbol{\gamma}^k = \left\{\gamma_1^k, ..., \gamma_{nL}^k\right\}$. This nonbinary spreading is low-rate mapping $\mathcal{M}: \mathbf{GF}(q) \to \mathbf{GF}(q)^L$, where each field symbol is exclusively mapped into a length-*L* vector over the same field. Field vector $\boldsymbol{\gamma}^k$ is transformed into length-(*snL*) bit vector $\mathbf{c}^k = \left\{c_1^k, ..., c_{snL}^k\right\}$ by mapping $\boldsymbol{\lambda}: \mathbf{GF}(q) \to \mathcal{X}^s, \mathcal{X} \triangleq \{1, -1\}$, where

each field symbol over GF(q) is mapped into s bits. User-specific interleaving π^k is performed to generate transmitted vector $\boldsymbol{x}^k$ to the Gaussian MAC. The user-specific interleaving is to make the transmitted data of each user random-like or to make the data of each user separable at the receiver as in the IDMA system [2]. Note that the nonbinary LDPC encoding and the nonbinary spreading can be the same for each user while the user-specific interleaving should be different for each user. The multiuser decoding is carried out by iteration, described in Section 2.1.

We give bit-error-rate (BER) Monte Carlo simulations of multiuser nonbinary SCCs [6]. We employ the (2, d)-regular nonbinary LDPC codes followed by length-L random spreading, i.e., mapping $\mathcal{M}$ for spreading is random generated. Note that the (2, d)-regular q-ary LDPC codes are empirically known as the best performing codes for $q \geq 64$. In the simulations, all the user-specific interleaves are random generated. We consider the 15-user 64-ary SCC with (d,L) = (3,17) and (3,20). The information bit length is fixed to 12000. The overall multiuser decoding iteration number is 50. We see that in Fig. 4 the gaps between the BER curves and their corresponding multiuser decoding thresholds obtained by our EXIT chart analysis [6] are about 0.6 and 0.77 dB at BER= 10^{-5} for the given information bit length, respectively. The multiuser decoding threshold is the minimum E_b / N_0 under which the decoding is error free. It should be emphasized that multiuser SCC with pair (3, 17), having the threshold of −0.34 dB, is only 0.31 dB away from Shannon bound −0.65 dB at the sum rate of 0.3.

3.2 Multiuser Parallel Concatenated Code

Another implementation of multiuser code is a multiuser parallel concatenated code (PCC). Fig. 3 illustrates the user k's encoder, consisting of M + 1 parallely concatenated component encoders with user-specific interleaver π^k employed [7].

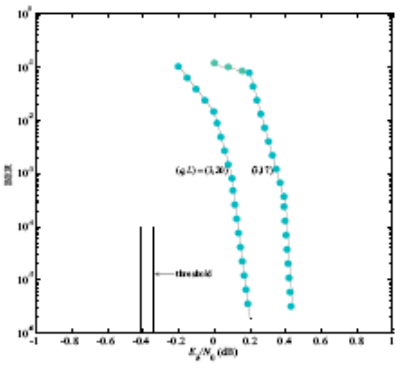

Fig. 4: BERs for 15-user 64-ary SCC with (d;L) = (3; 17) and (3; 20).

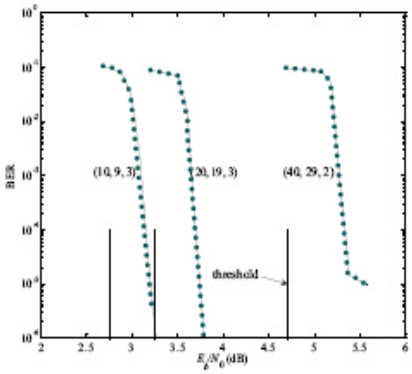

Fig. 5: BERs of K-user PCC with (K; q;M)=(10; 9; 3); (20; 19; 3), and (40,29,2)

Information vector $\mathbf{u}^k = \left(u_1^k, ..., u_N^k\right)$, $u_j^k \in \{0,1\}$, first crosses a parallel concatenated encoder, where the first component encoder is a rate-$(1/q)$ repetition encoder and the other M component encoders are the same rate-1 recursive convolutional (RC) encoder. Note that different interleavers π_i, $i = 1,\ldots, M$, should be employed before the RC encoders to make sure that the input vectors of each component encoder is different.

Output vector $\mathbf{c}^k = \left(\mathbf{u}_0^k, ..., \mathbf{u}_0^k, \mathbf{c}_1^k, ..., \mathbf{c}_M^k\right)$ with length $(q + M)N$ of these $M + 1$ component encoders is then interleaved by user-specific interleaver π^k into $\mathbf{x}^k = \left(x_1^k, ..., x_{(q+M)N}^k\right)$, which is transmitted to the Gaussian MAC. Here user-specific interleaver π^k should be different for each user to make sure that the transmitted vector of each user is from a different vector set. The iterative receive of the multiuser PCC is described in Section 2.1.

We give BER Monte Carlo simulations for the K-user PCCs [7]. In our simulations, the information vector length is 4096 and number of decoding iteration is 200.

To improve the BER performance for finitelength code, in our simulations the repetition encoder encodes each bit into a sequence with half 1's and half -1's. All the interleaves are randomly generated and the BER is averaged over all the possible interleaving realizations. In Fig. 5, we illustrated the BERs of three K-user PCCs with $(K, q, M) = (10, 9, 3)$, $(20, 19, 3)$, and $(40, 29, 2)$. Their accurate multiuser decoding thresholds are 2.75, 3.25, 4.71 dB by our fixed point analysis based on Gaussian approximation [7]. We see that all the BER curves converge to their thresholds well within a gap less than 0.8 dB at error rate 10^{-5}. It should be emphasized that multiuser PCC with (10,9,3) is only 1.58 dB away from Shannon bound 1.17 dB at the sum rate of 0.8333.

4. Conclusion

In this paper, we outlined multiuser coding for Gaussian multiple-access channel. We gave two examples of multiuser coding: multiuser nonbinary SCC and multiuser PCC. The common feature of two multiuser codes is that each user employs a repetition code as its component code, which is powerful in mitigating user interference. The multiuser decoding for these multiple-access systems is an iterative processing between multiuser detection and decoding. We showed that performance of these multiuser codes is close to theoretical limits by simulation and theoretical analysis.

One of our further works is to extend the multiuser binary PCC to nonbinary, and investigate its performance by comparing its multiuser decoding threshold with theoretical limit.

Acknowledgment

This work was partly supported by JSPS KAKENHI (24300030) Grant-in-Aid for Scientific Research (B).

References

1. K. Kusume, G. Bauch, and W. Utschick, “IDMA Vs CDMA: Analysis and comparision of two multiple access schemes,” IEEE Trans. Wireless Commun., vol. 11, no. 1, pp. 78–87, Jan. 2012.
2. P. Li, L. H. Liu, K. Y. Wu, and W. K. Leung, “Interleaving-division multiple-access,” IEEE Trans. Wireless Commun., vol. 5, no. 4, pp. 938–947, Apr. 2006.
3. G. Song, J. Cheng, and Y. Watanabe, “Maximum sum rate of repeat-accumulate interleave-division system by fixed-point analysis,” IEEE Trans. Commun., vol. 60, no. 10, pp. 3011–3022, Oct. 2012.
4. P. A. Hoeher and T. Wo, “Superposition modulation: myths and facts,” IEEE Commun. Mag., vol. 49, no. 12, pp. 110–116, Dec. 2011.
5. W. E. Ryan and S. Lin, Channel Codes: Classical and Modern, Cambridge, Cambridge University Press, 2009.
6. Y. Tsujii, G. Song, J. Cheng, and Y. Watanabe, “Approaching multiple-access channel capacity by nonbinary coding-spreading,” in Proc. IEEE ISIT, Istanbul, Turkey, July 7-12, 2013, pp. 2820-2824.
7. G. Song, J. Cheng, and Y. Watanabe, “K-user parallel concatenated code for Gaussian multiple-access channel,” in Proc. IEEE ICC, Budapest, Hungary, June 9-13, 2013, pp. 1879-1884..

Construction of Error-Correcting Signature Code on Hadamard Matrix

Shan Lu, Wei Hou, and Jun Cheng

Dept. of Intelligent Information Eng. & Sci., Doshisha University,
Kyoto, 610-0321 Japan
shanluxd@gmail.com, etl1703@mail4.doshisha.ac.jp,
jcheng@ieee.org

Abstract. Error-correcting signature code is used for user identification for multiple access adder channel. A construction of the error-correcting signature code on Hadamard matrix is proposed. The non-zero codewords of signature code are the rows of the signature matrix. In the coding scheme, a signature matrix is obtained from a Hadamard matrix by replacing every element by an initial signature matrix or its associated matrix depending on the element's binary value. The proposed code has longer length, higher decodability, and larger cardinality.

1. Introduction

In a multiple-access communication system, T users communicate with a single receiver through a multiple-access adder channel (MAAC) (Fig. 1) [1]. The input alphabet to the channel is integer set $K \triangleq \{0,1,2,\ldots k\}$, where k is a positive integer. When $Z_i \in K$, $i=1,2,\ldots,T$, are the channel inputs, channel output Y is given by $Y = Z_1 + Z_2 + \ldots + Z_T$, where + denotes real-number additions. Clearly, output Y belongs to $\{0,1, \ldots ,kT\}$, The channel is discrete and memoryless, and we assume synchronized transmission.

The MAAC shown in Fig. 1 is designated as a noiseless channel. When it is disturbed by noise, we describe it by putting a discrete memoryless channel just after the noiseless MAAC. This is often called a noisy MAAC [1], [2]. Here the discrete memoryless channel, which is set to $(kT + 1)$-ary input and $(kT + 1)$-ary output, is completely described by the transition probabilities for all possible input-output pairs (i, j), $0 \le i, \ j \le kT$.

For noisy MAAC, binary multi-user code was initially considered in [1] and extended to non-binary code [2]. However, these codes assume that all T users must be active. If the receivers do not know which users are idle in advance, then there exists a decoding ambiguity. To support a varying number of users over MAAC, all T users should share a zero codeword $\mathbf{0}^n$, where $\mathbf{0}^n$ is an n-vector (a row vector with length n) whose n elements are zero and a no-transmission (inactive) of the i-th user corresponds to sending $\mathbf{0}^n$.

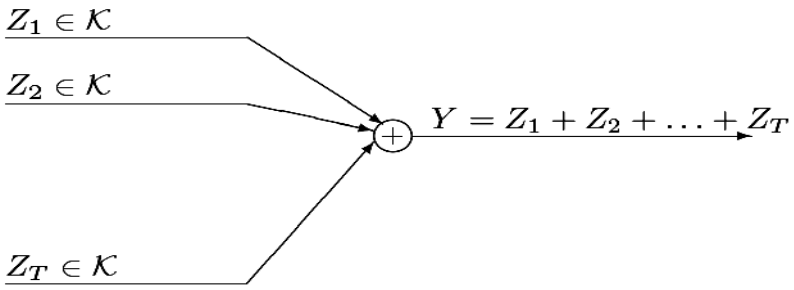

Fig. 1. T -user multiple-access adder channel with $K=\{0,1,2, \ldots ,k\}$

In this paper, we primarily construct a code for noise MAAC to support a varying number of users. In T -user multiple-access communication systems, the j-th user is assigned to codewords s_j and $\mathbf{0}^n$, where zero codeword $\mathbf{0}^n$ is shared among all T users. Active users send their non-zero codewords. The decoder receives a vector, which is the superposition of the transmitted codewords, and attempts to identify the active users. The set of the non-zero codewords of all T users is defined as the *signature code*, whose decodability guarantees unique identification of all active users through the MAAC, even if the received vector is disturbed by channel noise. The code designed to correct errors caused by channel noise and identify the status of users for the noisy MAAC is generally called error-correcting signature code.

The signature code is related to well-known problems of coin-weighting and sum-distinct sets in additive number theory [3,4,5,6,7,8]. The binary signature code is equivalent to Lindström's coin weighing designs [3], and a construction was given by Martirosyan and Khachatryan [4]. A generalized approach to construct binary signature code was previously proposed [5]. Non-binary code was originally considered by Jevtić [6,7] and extended to arbitrary code length [8]. The above signature codes were all recursively constructed. However, for each recursion, the minimum distance of the signature codes is maintained at one. Thus, these signature codes have no capability to correct errors.

In this paper, we give a construction of the error-correcting signature code on Hadamard matrix. The non-zero codewords of signature code are the rows of the signature matrix. In the coding scheme, a signature matrix is obtained from a Hadamard matrix by replacing every element by an initial signature matrix or its associated matrix depending on the element's binary value. The proposed code has longer length, higher decodability, and larger cardinality.

2. Definition

The *weight* of n-vector $\mathbf{y} = [y_1,y_2,...,y_n]$ is defined by $\omega(\mathbf{y}) = \sum_{i=1}^{n} |y_j|$, where y_i is an integer. The *distance* between vectors $\boldsymbol{y}$ and $\boldsymbol{y'}$ is defined by $d(\boldsymbol{y}, \boldsymbol{y'}) = \omega(\boldsymbol{y} - \boldsymbol{y'})$.

Definition 1 *For positive integer* δ, *set* $S = \{s_1, s_2, ..., s_T\}$, $s_i \in K^n$, is a δ-decodable signature code *if it holds* $\omega(u\mathbf{X}) \geq \delta$ *for any non-zero* T -vector $\mathbf{u} \in \{-1, 0, 1\}^T$, where X is the $T \times n$ *signature matrix*

$$X = [s_1, s_2, ..., s_T]^T \tag{1}$$

We denote by $(n, \delta, T)_k$ a δ-decodable $(k + 1)$-ary signature code with code length n and cardinality $T \triangleq |S|$. The sum rate of the signature code is $R = T/n$.

By Definition 1, the δ-decodable signature code implies that all possible 2^T sums of the transmitted vectors satisfy

$$d\left(\sum_{i=1}^{T} b_i s_i, \sum_{i=1}^{T} b'_i s_i\right) \geq \delta$$

for any two distinct T-vectors $\mathbf{b} = [b_1, b_2 ..., b_T]$ and $\mathbf{b}' = [b'_1, b'_2, ..., b'_T]$, where $b_i, b'_i \in \{0, 1\}$. According to multiuser coding [1] [2], a δ-decodable signature code for a noisy MAAC can correct $\lfloor (\delta - 1)/2 \rfloor$ or fewer errors, where notation $\lfloor p \rfloor$ stands for the greatest integer less than or equal to p. A $(n, \delta=1, T)_k$ code (or matrix) is considered *uniquely decodable* [3][4][8][9] and is used for noiseless MAACs so that the decoder can uniquely identify active users.

For preparation, a Hadamard matrix is described. For $j \geq 1$, Sylvester-type Hadamard matrix H_j with order 2^j is recursively constructed as [10]:

$$H_j = \begin{bmatrix} H_{j-1} & H_{j-1} \\ H_{j-1} & -H_{j-1} \end{bmatrix}, \quad with \quad H_0 = [1] \tag{2}$$

3. Main Theorem

In this section, we examine the generation of the construction of $(k + 1)$-ary signature code for a noisy MAAC.

Before going on, we define some notations. Let A and B be T_0 x n_0 matrices, where the elements in A and B belong to K. Let [A|B] be a T_0 x n_0 matrix related to matrices A and B. We define the operation:

$$h_{li} \overline{\otimes} [A|B] \triangleq \begin{cases} A & if \quad h_{li} = 1 \\ B & if \quad h_{li} = -1 \end{cases} \tag{3}$$

We also have $\left(-h_{li}\right)\overline{\otimes}\left[A\middle|B\right]=h_{li}\overline{\otimes}\left[B\middle|A\right]$

For $j \geq 0$, by Sylvester-type Hadamard matrix H_j of (2), we define matrix $X_j \triangleq H_j\overline{\otimes}\left[A\middle|B\right]$.

Here, matrix X_j is a $2^j T_0 \times 2^j n_0$ matrix obtained from H_j by replacing every element "1" by A and every element "-1" by B. The following theorem shows that matrix X_j gives a signature code with sum rate T_0/n_0:

Theorem 1 Let δ_a and δ_b be nonnegative integers, and $\delta_0 = \min\{\delta_a,\delta_b/2\}$. For all non-zero vectors $\mathbf{u}_0 \in \{-1,0,1\}^{T_0}$, if initial signature matrix A and its associated matrix B are satisfied

$$\omega(\mathbf{u}_0 A) \geq \delta_a \tag{4}$$

$$\omega(\mathbf{u}_0(A-B)) \geq \delta_b \tag{5}$$

then set Sj, which is composed of rows of matrix X_j of (1), is an

$$\left(n_j = 2^j n_0,\ \delta_j = 2^j \delta_0,\ T_j = 2^j T_0\right)_k \text{-signature code.}$$

We now consider a variation of matrices A and B.

Let $A' = \begin{bmatrix} O \\ A \end{bmatrix}$ and B' be $(T^* + T_0) \times n_0$ matrices, where O is a $T^* \times n_0$ zero matrix and $\boldsymbol{A}$ is a $T_0 \times n_0$ matrix. Let

$$X'_j = H_j\overline{\otimes}\left[A'\middle|B'\right] \tag{6}$$

We have the following corollary.

Corollary 1 Let δ_a and δ_b be nonnegative integers, and $\delta_0 = \min\{\delta_a,\delta_b/2\}$. For all vectors $[\mathbf{u}^*,\mathbf{u}^a]$, where $\mathbf{u}^* \in \{-1,0,1\}^{T^*}$, $\mathbf{u}^a \in \{-1,0,1\}^{T_0}$, if matrices A' and B' satisfy

$$\begin{aligned} &\omega\left(\left[\mathbf{u}^*,\mathbf{u}^a\right]A'\right) \geq \delta_a \quad for \quad \mathbf{u}^a \neq \mathbf{0}^{T_0} \\ &\omega\left(\left[\mathbf{u}^*,\mathbf{u}^a\right]\left(A'-B'\right)\right) \geq \delta_b \quad for \quad \left[\mathbf{u}^*,\mathbf{u}^a\right] \neq \mathbf{0}^{T^*+T_0} \end{aligned} \tag{7}$$

then set S'_j, which is composed of rows of matrix $\boldsymbol{X}'_j$ of (6) with the first T^* all-zero rows removed, is a

$$\left(2^j n_0, 2^j \delta_0, 2^j\left(T_0 + T^*\right) - T^*\right)_k \text{ -signature code.}$$

4. Signature Codes

Theorem 1 and Corollary 1 show that given any δ0-decodable code, with constraints (5) or (7), a $2_j\delta_0$-decodable code is obtained. Now we give two particular constructions.

4.1. (k + 1)-ary signature code

For any integer k, let $\ell=\lfloor \log_2 k \rfloor$, and define a $(\ell+1)\times 1$ matrix $\mathbf{a}=[2^0,2^1,...,2^{l-1},k]$. Note that matrix $\mathbf{a}^T$ is uniquely decodable [7], i.e., $\omega(\mathbf{u}\mathbf{a}^T) \geq 1$ with $\mathbf{u} \neq \mathbf{0}^{\ell+1}$, $\mathbf{u} \in \{-1,0,1\}^{\ell+1}$.Next we give a $(k+1)$-ary signature code from initial signature matrix $\mathbf{a}^T$.

Construction I Let $A=\mathbf{a}^T$ and $B=\mathbf{0}^{\ell+1}$ by Theorem 1. Set S_j, which is composed of rows of matrix X_j , is a $(2^j, 2^{j-1}, (\ell + 1)2^j)_k$-signature code since $\omega(\mathbf{uA}) \geq 1$ and $\omega(\mathbf{u(A-B)} \geq 1$.

Remark 1 The signature code in Construction I is originally from vector a^T, which is uniquely decodable for any positive integer k. It should be emphasized that a better choice may exist than a^T for a particular value of k. For instance, for k=7, uniquely decodable matrix $A=[3,5,6,7]^T$ gives a signature code with a sum rate of 4, which exceeds $a^T = [1,2,7]^T$

4.2. binary signature code

Before the construction, we give some definitions. For $t \geq 1$, we define matrices

$$A'_t = \begin{bmatrix} O_{t-1} & O_{t-1} \\ A'_{t-1} & A'_{t-1} \\ A'_{t-1} & B'_{t-1} \end{bmatrix} \quad and \quad B'_t = \begin{bmatrix} I_{t-1} & O_{t-1} \\ B'_{t-1} & B'_{t-1} \\ B'_{t-1} & A'_{t-1} \end{bmatrix} \tag{8}$$

with $A'_0 = [1]$ and $B'_0 = [0]$, where I_{t-1} is a $2^{t-1}\times 2^{t-1}$ identity matrix and O_{t-1} is a $2^{t-1}\times 2^{t-1}$ zero matrix. Matrices A'_t and B'_t have $T(t) = (t + 2)2^{t-1}$ rows and $n(t) = 2^t$ columns.

It follows that

$$A'_t - B'_t = \begin{bmatrix} -I_{t-1} & O_{t-1} \\ H_{t-1} & H_{t-1} \\ H_{t-1} & -H_{t-1} \end{bmatrix}$$

For $\mathbf{u}_t \in \{-1,0,1\}^{T(t)}$, and $u_t \neq \mathbf{0}^{T(t)}$, [1] showed that

$$\omega(\mathbf{u}_t(A'_t - B'_t)) \geq 1 \tag{9}$$

Note the weight of A'_t. In A'_t, sub-matrices O_{i-1} have 2^{i-1} all-zero rows. The number of all-zero rows in A'_t is the accumulation of the all-zero rows in O_{i-1} for i =1,2,...,t, i.e. $T^*(t) = 1+2+ ...+2^{t-1} =2^t -1$. Since we are only interested in the remaining (non-zero) rows of A'_t, we show by recursion that

$$\omega\left(\left[u_t^*, u_t^a\right] A_t'\right) \geq 1 \tag{10}$$

$$\text{for } u_t^a \in \{-1,0,1\}^{T(t)-T^*(t)} \quad and \quad u_t^a \neq \mathbf{0}^{T(t)-T^*(t)}$$

It is obvious that

$$\omega\left(\left[u_1^*, u_1^a\right] A_1'\right) \geq 1 \text{ for } \mathbf{u}_1^a \in \{-1,0,1\}^2 \quad and \quad \mathbf{u}_1^a \neq \mathbf{0}^2$$

Assuming that $\omega\left(\left[\mathbf{u}_{t-1}^*, \mathbf{u}_{t-1}^a\right] A_{t-1}'\right) \geq 1$ for any non-zero vector $\mathbf{u}_{t-1}^a \in \{-1,0,1\}^{T(t-1)-T^*(t-1)}$. Let $A_t = H_2 \otimes [A'_{t-1}|B'_{t-1}]$. Note that A_t is the sub-matrix of A'_t of (8). Since $\omega\left(\left[\mathbf{u}_{t-1}^*, \mathbf{u}_{t-1}^a\right]\left(A_{t-1}' - B_{t-1}'\right)\right) \geq 1$ (9), by Corollary 1, $\omega\left(\left[\mathbf{u}_{t-1}^*, \mathbf{u}_t^a\right] A_t'\right) \geq 1$ for $\mathbf{u}_t^a \in \{-1,0,1\}^{T(t)-T^*(t)}$ *and* $\mathbf{u}_t^a \neq \mathbf{0}^{T(t)-T^*(t)}$. Thus, we obtain (10).

Based on (9) and (10), from Corollary 1, we have the following construction of a binary signature code:

Construction II Set S_j, which is composed of rows of matrix $X_j' = H_j \overline{\otimes}\left[A_t' \middle| B_t'\right]$ where the first 2^t-1 rows were removed, is a $\left(2^{j+t}, 2^{j-1}, (t+2)2^{j+t-1} - 2^t + 1\right)_k$-signature code.

The sum rate of the above binary signature code is $R = \dfrac{(t+2)2^{j+t-1}+1}{2^{j+t}} > 1$, $j,t \geq 1$. This means that it is higher than that of the code in Construction I when $k = 1$

Conclusion

Error-correcting signature code is used for user identification for multiple access adder channel. We gave a construction of the error-correcting signature code on Hadamard matrix. The non-zero codewords of signature code are the rows of the signature matrix. In the coding scheme, a signature matrix is obtained from a Hadamard matrix by replacing every element by an initial signature matrix or its associated matrix depending on the element's binary value. The proposed code has longer length, higher decodability, and larger cardinality..

Acknowledgment

This work was partly supported by JSPS KAKENHI (24300030) Grant-in-Aid for Scientific Research (B).

References

1. S. C. Chang and E. J. Weldon, Jr., "Coding for T -user multiple-access channels," *IEE*E *Trans*. *Inform*. *Theory*, vol. IT-25, no. 6, pp. 684–691, Nov. 1979.
2. J. Cheng and Y. Watanabe, "Multi-user *k*-ary code for noisy multiple-access adder channel," *IEE*E *Trans*. *Inform*. *Theory*, vol. IT-47, no. 6, pp. 2603-2607, Sept. 2001.
3. B. Lindstr¨om, "Determining subsets by unramified experiments," in A *Survey of statistica*l *Desig*n *an*d *Linea*r *Models*, ed. J. N. Srivastava, North-Holland, New York, 1975.
4. S. S. Martirosyan and G. G. Khachatryan, "Construction of signature codes and the coin weighing problem," *Probl*. *Inform*. *Transm.*, vol. IT-25, pp. 334-335, Oct.-Dec. 1989.
5. W. H. Mow, "Recursive constructions of detecting matrices for multiuser coding: a unifying approach," *IEE*E *Trans*. *Inform*. *Theory*, vol. IT-55, no. 1, pp. 93-98, Jan. 2009.
6. D. Jevti´c, "Disjoint uniquely decodable codebooks for noiseless synchronized multiple-access adder channels generated by integer sets," *IEE*E *Trans*. *Inform*. *Theory*, vol. IT-38, No. 3, pp. 1142–1146, May 1992.
7. D. Jevti´c, "On families of sets of integral vectors whose representatives form sum-distinct sets," SIAM , J. Discrete Math., vol. 8, no. 4, pp. 652-660, Nov. 1995.
8. J. Cheng and Y. Watanabe, "T -user code with arbitrary code length for multiple-access adder channel," IEICE Trans. Fundamentals, vol. E82-A, no. 10, pp. 2011–2016, Oct. 1999.
9. T. Bohman, "A sum packing problem of Erd˝os and the Conway–Guy sequence," Proc. Amer. Math. Soc., vol. 124, no. 12, pp. 3627–3636, Dec. 1996.
10. F. J. MacWilliams and N. J. Sloane, The Theory of Error-Correcting Codes, Amsterdam, The Netherlands: North-Holland, 1977.

The Experimental Study of Target FSR Shadow Detection using GPS signals

Hristo Kabakchiev[1], Ivan Garvanov[2], Vera Behar[3], Andon Lazarov[4], and Hermann Rohling[5]

[1]Sofia University, Sofia, Bulgaria
ckabakchievr@fmi.uni-sofia.bg

[2] ULSIT, Sofia, Bulgaria
i.garvanov@unubit.bg

[3] IICT-BAS, Sofia, Bulgaria
behar@bas.bg

[4] BFU, Burgas, Bulgaria,
lazarov@bfu.bg

[5] TU hamburg-Harburg, Hamburg,Germany
rohlingr@tu-harburg.de

Abstract. In this paper, some experimental results are analyzed, which are obtained using a moving car-based GPS-FSR system. The GPS receiver mounted at a car records signals from concrete satellites, when a car moves along stationary ground objects (building, bridge).

1. Introduction

Forward Scattering Radar (FSR) is a specific type of bistatic radars that operate in the narrow area of the forward scattering effect where the bistatic angle is close to 180^0, and the target moves near the transmitter-receiver baseline [1]. In FSR, the Babinet principle is exploited to form the forward scatter signature of a target. Due to the forward scattering effect, the Radar Cross Section (RCS) of targets extremely increases (by 2-3 orders) and mainly depends on the target's physical cross section and is independent of the target's surface shape and the absorbing coating on the surface. In this paper a passive Forward Scatter Radar (FSR) system, in which GPS satellites are exploited as non-cooperative transmitters, is studied (Fig. 1). The civil L1 signal is transmitted by satellites at 1572.42 MHz and contains the coarse acquisition (C/A) code, which is unique for each satellite. The idea to apply a GPS L1 receiver to FSR for air target detection is discussed in [2]. Some experimental results of a GPS L1 receiver concerning the detection of air targets are shown and discussed in [3]. A possible algorithm for air target detection in a GPS L5-based FSR system is described in [4], and the detection probability characteristics are calculated in [5] in case of low-flying and poorly maneuverable air targets in the urban interference environment. The aim of this study is to verify the possibility to detect FSR shadow

of ground targets by a GPS L1 FSR system when GPS satellites are located at small elevation angles.

The experimental scenario includes a moving car-based GPS-FSR system that registers FSR shadow of a stationary ground object. In such a system, the signal integrated at the output of the Code&Carrier tracking block (message bits) of a GPS receiver can be used for detection of the FSR shadow created by ground targets. In this paper we propose to additionally integrate the output signals from M visible satellites in order to improve the SNR before detection. Target detection is indicated if the signal integrated from M satellites exceeds a predetermined threshold.

2. FSR experiment description

The topology of the experimental system is shown in Fig.1. In this experimental study, the GPS L1-based recording system is mounted at a car. As usual, near 7-8 satellites are visible, however, in our experiment only the strongest signals from three visible satellites are performed to detect a target FSR shadow. During the experiment, a car with GPS receiver (GNSS_SRR) moves with a certain velocity (60-70 km/h) under two bridges, small and large, which are used as a source of FS shadow.

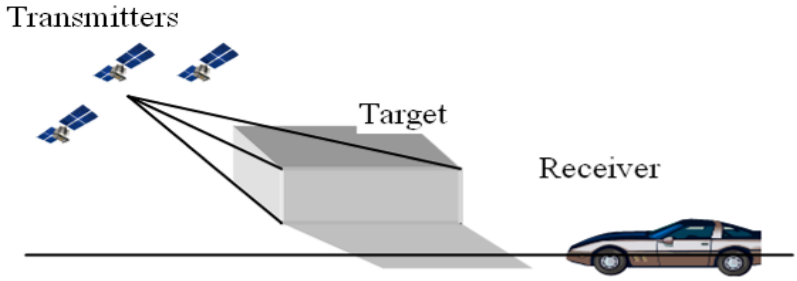

Fig. 1. FSR topology

3. Signal processing

The general block-scheme of a possible algorithm for FSR shadow detection using several (M) visible satellites is shown in Fig 2. According to this block-scheme, several visible GPS satellites are acquired and tracked over the complete duration of recorded signals. We consider the case when the acquisition and tracking algorithms of a GPS receiver are implemented in MATLAB. The absolute values of the *Ip* component at the output of the Code&Carrier tracking block are then integrated during *N* milliseconds. These integrated output signals from M satellites are additionally summed in order to improve SNR before detection. Target detection is indicated if the signal integrated from M satellites exceeds a predetermined threshold H.

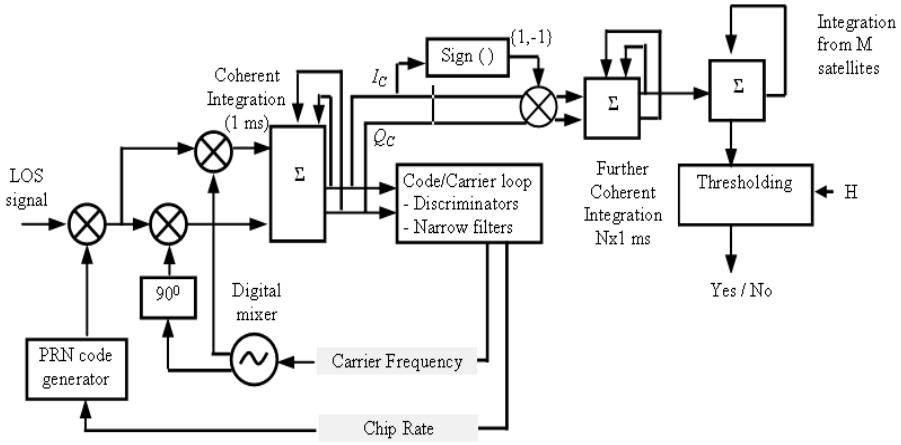

Fig.2. Signal processing used for target detection in a passive FSR using GPS signals from M satellites

4. Experimental results

During the first experiment, a car with GPS receiver moves with a constant velocity of 60 km/h under the small bridge (Fig. 3). The signals received by the GPS receiver are stored and next are performed by programs of a software GPS receiver implemented in MATLAB. In our case the signal performance for shadow detection includes only four stages: C/A code acquisition, Carrier&Code tracking, coherent integration in time and non-coherent integration from M satellites. The output of C/A code acquisition performance is shown in Fig. 4. It can be seen that during this experiment seven satellites are visible, three of which with numbers 12, 29 and 25 have the strongest signals. The signals from these satellites will be used for detection of the FS shadow created be a bridge. The output signals of the Carrier&Code tracking block of these satellites, i.e. the navigation messages, are shown on Fig. 5-7. Next, these signals are integrated during 200*ms*.

Fig.3. Experimental scenario

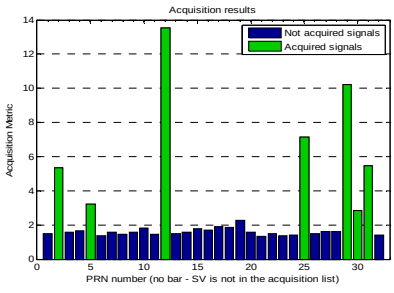

Fig. 4. Satellite constellations

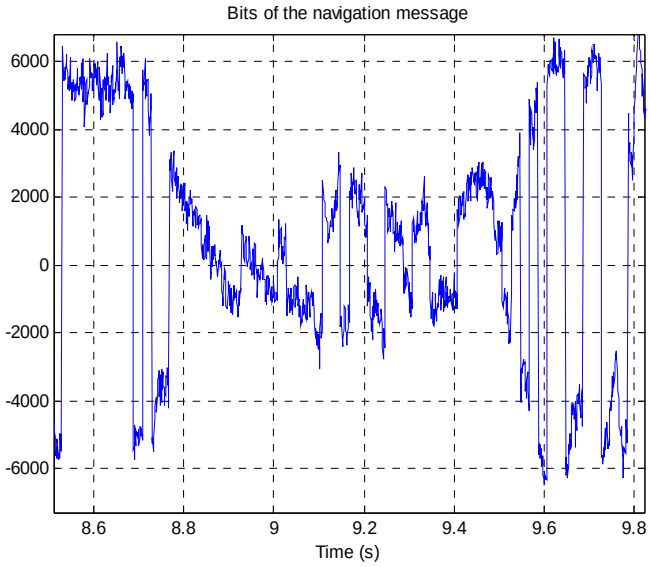

Fig 5. Navigation message of satellite 12

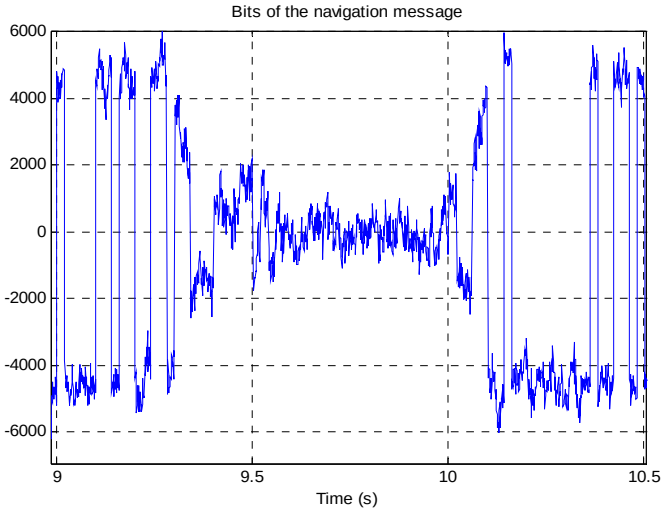

Fig 6. Navigation message of satellite 29

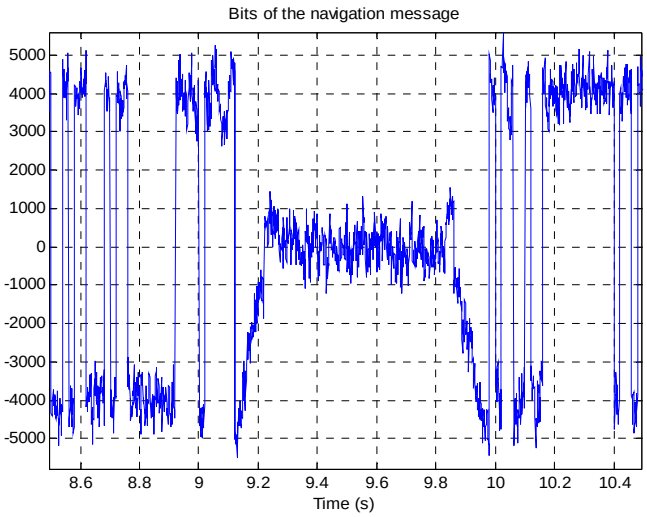

Fig 7. Navigation message of satellite 25

The integrated signals from these satellites are shown on Fig. 8. In order to improve SNR, the integrated signals from each of satellites are summed, and the summed signal is compared with a predetermined threshold in order to indicate detection of FSR shadow. The integrated signal from three satellites together with the threshold of 110 dB is shown in fig. 9. It can be seen that the SNR of 10 dB is sufficient in order to detect the FS shadow of a bridge.

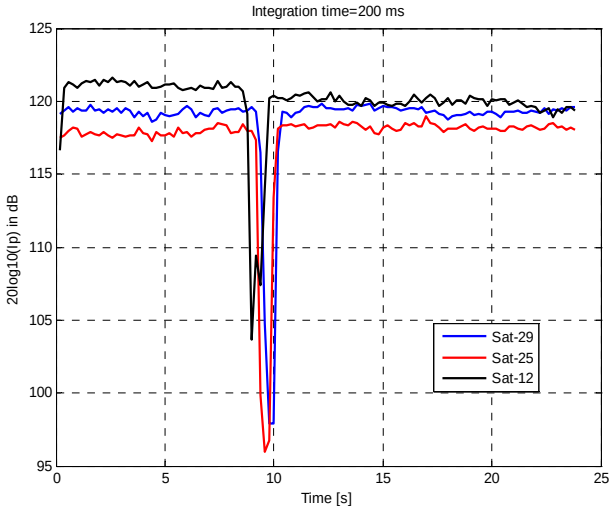

Fig.8. Integrated power (200ms)

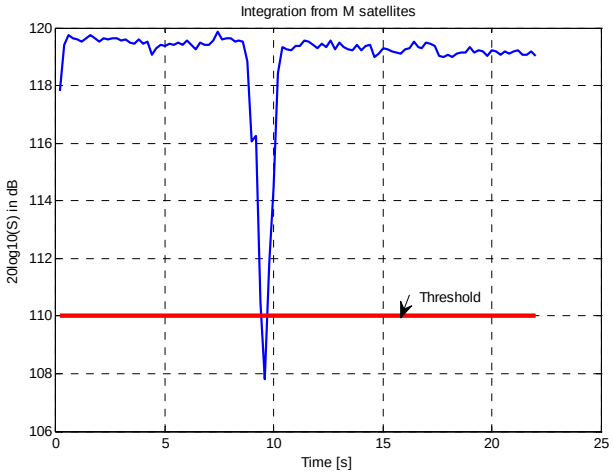

Fig. 9. Integrated power from three satellites

In the second experiment, the large bridge is a combination of two parallel narrower bridges with a distance of 5-6 m between them. The car with a GPS receiver moves under two bridges as shown on Fig. 10. The output of the C/A code acquisition is shown in Fig. 11. Eight satellites are visible, and satellites 12, 29 and 25 have the strongest signals. The output signals of the Carrier&Code tracking block of these satellites, i.e. the navigation messages, are shown on Fig. 12-14. Next these signals are integrated during 200ms. The integrated signals of these satellites are shown on Fig. 15. In order to improve SNR, the integrated signals from each of satellites are summed. Next the summed signal is compared with a predetermined threshold in order to indicate detection of the bridge FSR shadow.

Fig.10. Experimental scenario

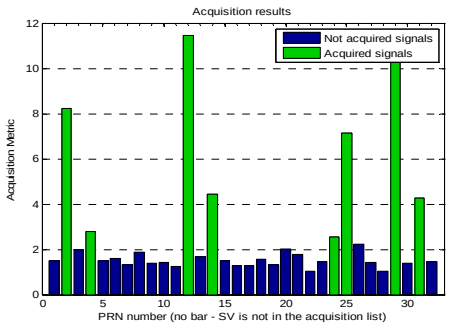

Fig. 11. Satellite constellations

The integrated signal from three satellites together with the threshold of 110 dB is shown in Fig. 16. It can be seen that the SNR of 10 dB is sufficient in order to detect the FS shadow of two parallel bridges.

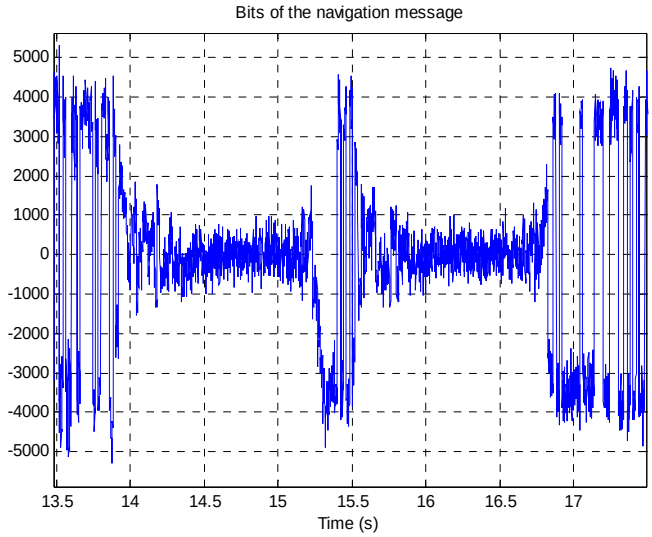

Fig 12. Navigation message of sat. 12

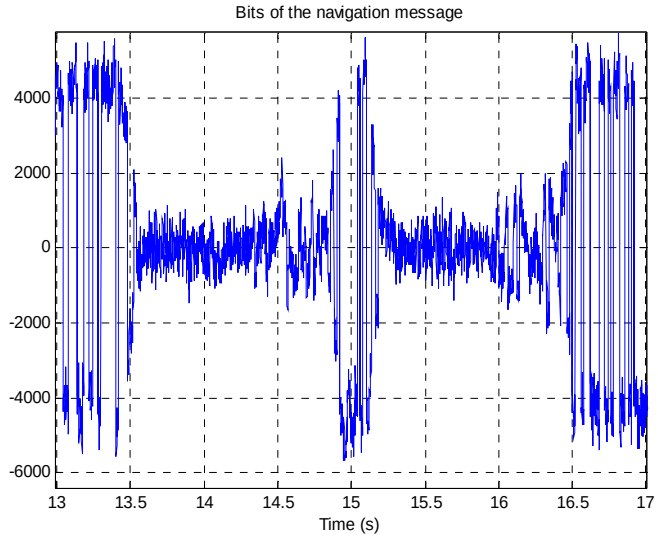

Fig 13. Navigation message of sat. 29

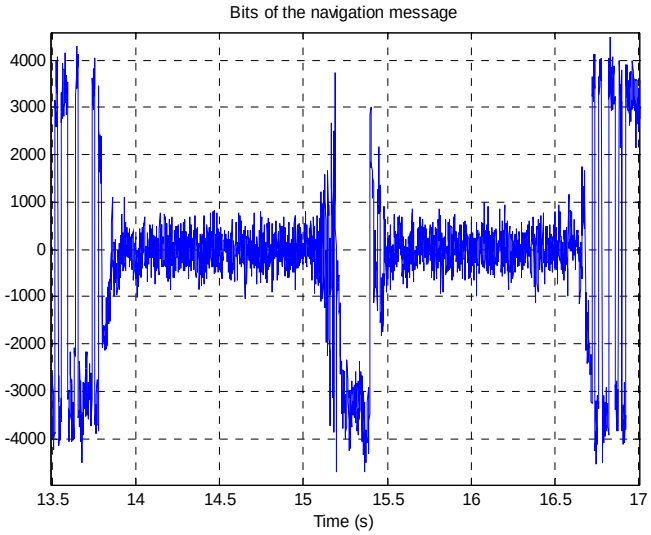

Fig 14. Navigation message of sat. 25

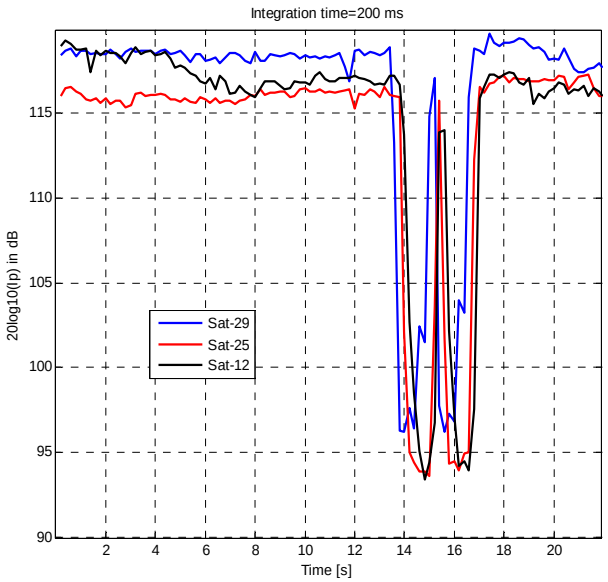

Fig.15. Integrated power (200ms)

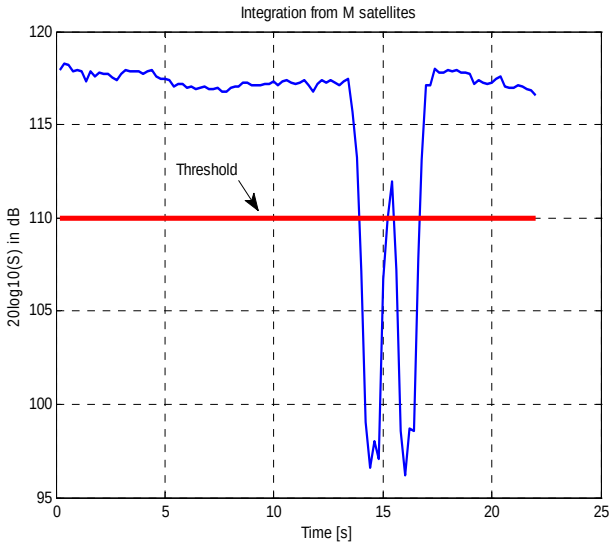

Fig. 16. Integrated power from three satellites

5. Conclusions

It is shown that a GPS L1 FSR system can be used for detection of FSR shadows from stationary ground objects. For FSR shadow detection, such a system uses integration of signals at the output of a Code&Carrier tracking block and integration of signals from several satellites.

Acknowledgements

This work is partly supported by the project AComIn "Advanced Computing for Innovation", grant 316087, funded by the FP7 Capacity Program (Research Potential of Convergence Regions) and projects DTK 02/28.2009 and NIP-02-2013.

References

1. M. Cherniakov (ed.), “Bistatic Radar: Principles and Practice”, Wiley & Sons, 2007.
2. V. Koch, R. Westphal, “New approach to a multistatic passive radar sensor for air/space defense”, IEEE AES Systems Magazine, pp. 24-32, November 1995.

3. I. Suberviola, I. Mayordome, J. Mendizabal, "Experimental results of air target detection with GPS forward scattering radar, 2012, In IEEE Geoscience and Remote Sensing Letters, vol. 9, no. 1, pp.47-51 January 2012.
4. V. Behar, Chr. Kabakchiev, "Detectability of Air Target Detection using Bistatic Radar Based on GPS L5 Signals", Proc. IRS'2011,12-th Intern. Radar Symp., Leipzig, pp. 212-217, September 2011.
5. V. Behar, Chr. Kabakchiev, H. Rohling," Air Target Detection Using Navigation Receivers Based on GPS L5 Signals", Proc. of ION GNSS' 2011, 24th International Technical Meeting of The Satellite Division of the Institute of Navigation, Portland OR, pp. 333-337, September 2011.

Study of Radio Waves Propagation into Buildings

Emil Altimirski and Petko Simeonov

Faculty of telecommunications, Technical University – Sofia, Bulgaria
edit12@abv.bg, psimeonov@tu-sofia.bg

Abstract. This paper provides an overview of methods for modeling of indoor radio-wave propagation, and concentrates on the ray-tracing modeling technique because of its practical appeal and its applicability for implementation of System for Monitoring and Management of Energy Efficiency (SMMEE) in public buildings using radio communications.

1. Introduction

The monitoring and management of the energy efficiency in public buildings can be exanimated as complex system combining two major parts – hardware and software modules for remote monitoring and control. The first part was designed and implemented by the research laboratory "Radio control and environmental monitoring" of the Department of Telecommunications at the Technical University in Sofia. It is designed to monitor and control certain parameters into buildings and send the measured data to the central management system.

The sensor modules are compact, low cost devices which are placed in each room in the controlled building. They are battery supplied and does not require connection to any power grids or computer networks. The battery power ensures operation of the module for at least 10 years. Each sensor module measures the temperature, lighting in the room, opening the door/window and the status of its own battery. It has a low-powered transmitter in the range of 433 MHz, which transmits information to the hub, located in the corridor or in the immediate area. The information is transmitted in certain periods or when is detected significant change in the measured parameters.

The communication subsystem of the SMMEE is developed for optimization of technical and economic parameters, as well as easy installation and maintenance. It combines three different technologies - VHF-radio, GSM-GPRS-channel and wire channels.[1]

For great importance for the successful implementation of the SMMEE in different types of buildings is the understanding the nature of electromagnetic-wave propagation in an indoor environment. Development of reliable and cheap method for modeling the indoor radio propagation, applicable for different types of buildings will facilitate the process of implementation and installation of the SMMEE into the public buildings.

The indoor environment is susceptible to interference. The effects of reflection, refraction and scattering of the radio waves by different structures inside the buildings, cause the transmitted signal to reaches the receiver by more than one path,

this phenomenon is called a multipath fading. The multipath propagation of the radio waves leads to deep fading and pulse spreading of the signal, this is very undesirable in one digital radio system like the SMMEE, because it can produce inter symbol interference and can seriously degrade system's performance.

Critical issue for achieving good propagation performance and hence achieving better connectivity for indoor wireless networks is selecting the position of the transmitters. For better positioning of the transmitters is needed good characterization of the multipath medium. The characterization of the propagation medium of every building by taking radio propagation measurements is difficult and expensive. For that reason the interest in developing a reliable propagation model for prediction of the propagation characteristics applicable for the indoor environment is very high.

The existing propagation models for characterization of the indoor radio propagation can be classified into two major classes: statistical models and site-specific propagation models.[2]

2. Indoor radio propagation

Indoor environment protects the radio channels from effects like snow, rain, hail, clouds or temperature inversion and etc. common for the outdoor radio channels, but because of the variation of building size, shape, structure, layout of rooms and most importantly, the type of construction materials, the propagation of electromagnetic-waves inside a buildings has more complex multipath nature than that of an outdoor mobile radio channels. It is well known that the radio wave propagation inside a factory building is quite different to propagation in office building both differs on its structure and in the materials used. The variation of type of materials used in internal partitions, outside walls, ceilings and floors, as well as the size and percentage of windows, age of buildings, people density and activity are also factors which influence the indoor electromagnetic-wave propagation.

Path loss The spatial distribution of the power of a transmitter, in general is a decreasing function of the distance d from the transmitter. This function is represented by a distance power law of the form $P=1/d^m$. For free space, m is equal to 2 and for that case it is said that the power gain follows an inverse square law. In an indoor environment this is not valid anymore. In [3,4] it is shown that when the transmitter and the receiver are paled in same premise, in sight of each other, the power decrease with a value of m ranging of 1.5 to 1.8, when the receiver is located within a room off the premise, with no line-of-sight, m ranged from 3 to 4.

The pathloss depends also on the frequency of the signal, it is great at higher frequency. The measurements results in [5] indicates that loss thought floors is greater at the higher frequency. The wavelengths in the millimeter range cannot penetrate most common building materials such as brick and concrete block and that signal attenuation occurs more rapidly with distance.

In [6,7] are given the values of m according to the used building materials. The signal attenuation in buildings depends on the type of the used construction materials.

Fading properties The typical architecture of one indoor radio system includes fixed base station antenna installed in an elevated position, that communicate with a

number or mobile or fixed radio devices inside the building. In this scenario, due to the reflection, refraction and scattering of radio waves by different structures inside the building, the radio signal usually reaches the receiver by more than one path, resulting in an effect called multipath fading as shown in Fig 1. The received signal is distorted version of the transmitted signal, result of combining the signal components arriving from the indirect paths and the direct path signal (if it exists). In narrow-band transmission, the multipath medium causes fluctuation in the envelope and phase of the received signal. In wide-band pulse transmission, the result of multipath fading is a series of delayed and attenuated pulses, for each transmitted pulse.

If no dominant signal path (line-of-sight) exists between the receiver and transmitter, and continuous-wave signal transmission, the statistics of the received signal envelope can be descripted by a Rayleigh distribution function. If there is line-of-sight between the transmitter and the receiver, or one of the signal paths is dominant, the statistics of the signal envelope are Rician.

In case of digital pulse transmission the delay spread of a multipath signal affects the data transmission rate. The temporal spread of the channel is described by the parameters the mean excess delay, the RMS delay spread and the excess-delay spread.

- *Mean excess delay spread - describes the average propagation delay relative to the first arriving signal component*
- *The RMS delay spread measures the temporal spread of the power delay profile about the mean excess delay.*
- *The excess-delay spread (X dB) indicates the maximum delay, relative to the first-arriving signal component, at which the multipath energy falls to X dB below the peak received level.*

Delay spreads are affected by used construction materials, building age, wall locations and ceiling heights. Buildings with more metal material have larger delay spreads.

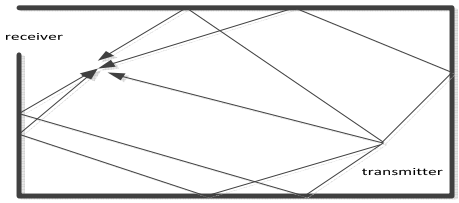

Fig. 1 Multipath propagation

3. Indoor propagation modeling

There are two main classes of indoor radio propagation models – statistical and site-specific – both can be used for design and installation of indoor radio systems and both shows strengths and weaknesses.

Statistical models Firstly statistical impulse-response model for the multipath fading propagation, was suggested in [8,9] for outdoor environment, and subsequently it was transformed for indoor radio channel propagation modeling. In [3] are used measurement results for several types of indoor environments in order to simulate and analyze various indoor communication schemes. The model assumes that the

multipath components arrive in clusters. The received amplitude of each component is an independent Rayleigh random variable, with a variance that decays exponentially with propagation delay, as well as with time delays, within the cluster. The corresponding phase angles for each component are independent uniform random variables over (0.2π) . The clusters and multipath components within a cluster from a Poisson-arrival process with different rates. The multipath components and the clusters have exponentially distributed inter-arrival times. The formation of the clusters is related to the building structure, while the multipath components within each cluster are formed by multiple reflections from objects in the vicinity of the transmitter and the receiver. The model has enough flexibility to permit reasonably accurate fitting of the measured channel responses and is simple enough to simulation.

A statistical model for indoor radio propagation, based on performed measurements of 12000 impulse response profiles of the channels collected in different office buildings is developed in [10,11] In this model, the data arrival time is modeled as a modified Poisson distribution and the amplitudes were found to lognormal-distributed over both local and global areas, with a log-mean value that decreases almost linearly with increasing excess-delay. A radio coverage prediction model, based on a few building parameters is formulated in [12], the model provides a quick and simple way to predict the pathloss, in decibels. It is useful for an initial coverage prediction for indoor environment, but it only provides path loss information and may not work well in complex indoor structures.[13] proposes models based on a simple d^n exponential path loss against distance relationship. In open-plan buildings, the path loss exponent n is close to 2. For environments with many more obstructions between the transmitter and the receiver, the exponent can be much higher. Statistical distance-dependent path loss models are useful for understanding the propagation of radio waves in buildings, but there are needed a lot of measurements to obtain enough data to determine the appropriate parameters to model a particular type of indoor environment.

Site-specific propagation models This class propagation models are based on electromagnetic-wave propagation theory to characterize indoor radio propagation. Unlike statistical models, site-specific propagation models do not relay on extensive measurement, but a greater detail of the indoor environment is required to obtain an accurate prediction of signal propagation inside a building.

In theory, electromagnetic-wave propagation characteristics could be exactly computed by solving Maxwell's equations with the building geometry as boundary conditions, but this requires very complex mathematical operations and huge computing power and it is not very economical. For these reasons approximate numerical methods are of interest. Ray tracing is an intuitively appealing method for calculating radio signal strength, time-invariant impulse response, RMS delay spread and related parameters in an indoor environment. [14,15]

The concept of ray-tracing modeling is based on the fact that high-frequency radio waves behave in a ray-like fashion and signal propagation can be modeled simple as ray propagation. Rays can be launched from a transmitter location and the interaction of the rays with the obstacles within a building can be modeled using well-known reflection and transmission theory. Two types of ray-tracing methods can be used - the "image" and the "brute-force" ray-tracing methods. For scatters bounded by plane

faces it is convenient to employ the image method to mirror the radio wave source at a particular face. The point where the mirror face intersects the line connecting the transmitter image and the receiver is the point at which specular reflection occurs. This method is well suited to radio propagation analysis in the case of geometries of low complexity and where a low number of reflections are considered.

The brute-force ray-tracing method considers a bundle of transmitted rays that may or may not reach the receiver. The number of rays employed and the distance from the transmitter to the receiver location determine the available spatial resolution and hence the accuracy of the model. This method requires more computing power than the image method. Ray tracing can be much less demanding of computation than methods based on Maxwell's equations. Reliable site-specific ray-tracing propagation prediction models for each building based on its detailed geometry and construction can be very effective tools in designing indoor communication systems.

4. Modeling by ray tracing

The ray-tracing method computes the scattering of electromagnetic waves by simple reflection and refraction.

The degree of transmission and reflection of a signal through and from an obstacle is related to the complex permittivities of the obstacle.

Transmission and reflection of a radio signal When a signal is transmitted through or reflected from a wall or a surface, the degree of signal attenuation and the amount of phase change depend on the complex transmission and reflection coefficients which are computed from the complex permittivities of the materials the signal rays come across. Other factors affecting the transmission and reflection of the signal are the angle of incidence and the relative polarization of the electromagnetic-wave.

The ratio of the transmitted to the incident electric-field strengths determines the complex transmission coefficient and the ratio of the reflected to the incident electric-field strengths define the complex reflection coefficient.

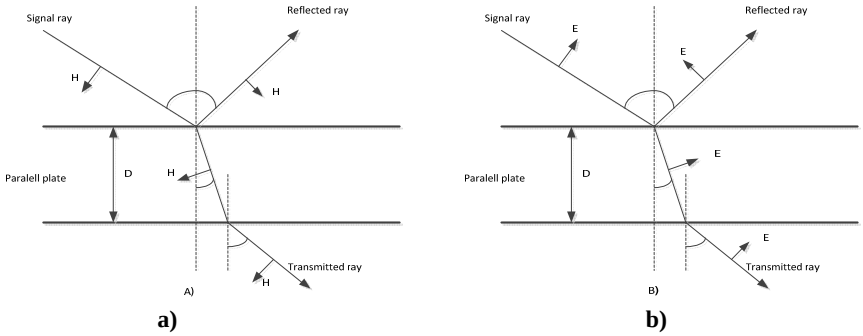

a) **b)**

Fig. 2 A signal wave incident obliquely on a parallel plate

On Fig 2 is considered the scenario where the ray is incident on a parallel plate, which may be a partition or a wall, there are two cases:

Fig. 2a the signal has a horizontal polarization with reference to the parallel plate. The complex transmission and reflection coefficients for horizontal polarisation are:

transmission coefficient:
$$t = \frac{E_t}{E_i} = \frac{2\cos\phi_1}{\cos\phi_1 + \left(\frac{\varepsilon}{\varepsilon_0} - \sin^2\phi_1\right)^{1/2}} \tag{1}$$

refraction coefficient:
$$\gamma = \frac{E_r}{E_i} = \frac{\cos\varphi_1 - \left(\frac{\varepsilon}{\varepsilon_0} - \sin^2\varphi_1\right)^{1/2}}{\cos\varphi_1 + \left(\frac{\varepsilon}{\varepsilon_0} - \sin^2\varphi_1\right)^{1/2}} \tag{2}$$

Fig. 2b the signal is polarized vertically with respect to the parallel plate. The complex transmission and reflection coefficients for vertical polarization are:

transmission coefficient:
$$t = \frac{E_t}{E_i} = \frac{2\cos\varphi_1}{\left(\frac{\varepsilon}{\varepsilon_0}\right)^{1/2}\cos\varphi_1 + \left(1 - \frac{\varepsilon}{\varepsilon_0}\sin^2\varphi_1\right)^{1/2}} \tag{3}$$

refraction coefficient:
$$\gamma = \frac{E_r}{E_i} = \frac{\frac{\varepsilon}{\varepsilon_0}\cos\varphi_1 - \left(\frac{\varepsilon}{\varepsilon_0} - \sin^2\varphi_1\right)^{1/2}}{\frac{\varepsilon}{\varepsilon_0}\cos\varphi_1 + \left(\frac{\varepsilon}{\varepsilon_0} - \sin^2\varphi_1\right)^{1/2}} \tag{4}$$

where: e is the complex permittivity of the parallel plate , ε_0 is the permittivity of free space
u_1 is the angle of incidence
E_i is the incident electric field strength, E_r is reflected electric field strength
E_t is transmitted electric field strength

When a signal ray, meets a parallel plate (a wall or partition) with thickness D the signal is attenuated while going through the material. The complex transmission coefficient is then given as

$$E_t^{'}/E_i = t_c e^{-ad} \tag{5}$$

where $t_C = t_A \times t_B$ is a complex transmission coefficient
t_A - the complex transmission coefficient at A
t_B - the complex transmission coefficient at B
α - attenuation factor
d - the distance travelled by a signal ray in the material

The attenuation factor α, is given from:

$$\alpha = \frac{2\pi}{\lambda}\left\{\frac{\varepsilon_r'}{2}\left|\left[1 + \left(\frac{\varepsilon_r''}{\varepsilon_r}\right)^2\right]^{1/2} - 1\right|\right\}^{1/2} \tag{6}$$

where: ε_r' - real part of the relative complex permittivity of the material

ε_r'' - imaginary part of the relative complex permittivity of the material

λ– wave length of the signal

Line-of-sight signal strength calculation

The received signal strength at the receiver from a line-of-sight path is given by:

$$E_{LOS} = \frac{t_c E_s e^{-j2\pi d_0/\lambda}}{d_0} \tag{7}$$

where: E_s – the source signal strength from the transmitter to receiver
t_c – complex transmission coefficient, λ – wave length of the signal

On Fig 3 is shown a first order path of the signal, the signal strength is given by:

$$E_{1R} = \frac{r_c t_c E_s e^{-j2\pi(l_1+l_2)/\lambda}}{(l_1+l_2)} \tag{8}$$

Fig. 4 shows a second order reflection path, the signal strength is given by:

$$E_{2R} = \frac{(r_{c1}r_{c2})(t_{c1}t_{c2})E_s e^{-j2\pi(l_1+l_2+l_3)/\lambda}}{l_1+l_2+l_3} \tag{9}$$

and the multiple reflection signal strength at the receiver is given by:

$$E_{mR} = \frac{(r_{c1}r_{c2}...r_{cm})(t_{c1}t_{c2}...t_{cn})E_s e^{-j2\pi(l_1+l_2+l_3...+l_{m+1})/\lambda}}{l_1+l_2+l_3+...+l_m} \tag{10}$$

where: *Es* – signal strength from the transmitter
E_{1R} – first order reflected signal strength at the receiver
E_{2R} – second order reflected signal strength at the receiver
E_{mR} – multiple reflection signal strength at the receiver
$l_1 + l_2 + ... + l_k$, k any positive integer – total reflection distance
$r_{c1}, r_{c2},..,r_{cm}$ – complex reflection coeficents,
$t_{c1}, t_{c2},..,t_{cn}$ – complex transmission coefficient
λ – wavelenght of the signal

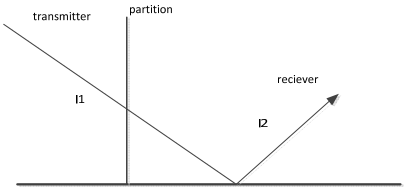

Fig. 3 First order reflected signal

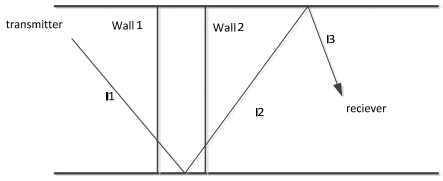

Fig.4 Second order reflected signal

Ray-tracing method In ray-tracing methods, the locations of transmitters and receivers are assigned to points referenced by three dimensional co-ordinates. The walls, partitions, ceilings and floors in an indoor environment are usually modelled as plane surfaces of given thickness and complex permittivity. For simplication, curved surfaces can be modelled as piecewise planar surfaces. The rays from the transmitter antenna are reflected off walls, partitions, ceilings, floors and tables etc. or transmitted through walls and partitions etc. to arrive at the receiver. As already

mentioned, two common methods - the image method and the brute-force method - have been developed to trace the rays from the transmitter to the receiver.

(a) ***Image method:*** [14,16] This method assumes every plane face in an indoor environment to be a mirror. For line-of-sight propagation, it is easy to trace the ray by connecting the transmitter and receiver. For single reflection propagation, the radio source is mirrored at a particular face. The point of intersection of the mirror face and the line connecting the transmitter image to the receiver is the point where specular reflection occurs. The single-reflection propagation path can then be obtained by connecting the source point, reflection point and receiver point. For repeated reflection, the image of the radio source with reference to a particular plane face is found first. The next step is to find an image of the source image with reference to another plane face where the second point of reflection will be located. Following the same rule, all the points of reflection at the relevant plane faces can be obtained. The multiple-reflection propagation paths can then be obtained. The method described above, starting at the source image, is referred to as the forward ray-tracing method. It is also possible to be start at the receiver image and trace back to the transmitter. This is called the backward ray-tracing method.

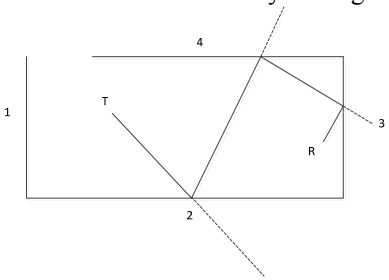

Fig. 5 Using images to trace a three reflection path

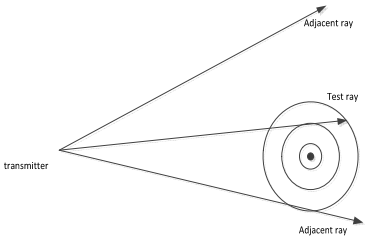

Fig. 6 Two-dimensional view of the reception sphere.

Consider a rectangular room as shown in Fig. 5. The transmitting antenna is located at point T, while the receiving antenna is located at point *R*. To trace the path from T to *R***,** reflecting off walls 2, 4 and 3, three images have to be found. First the first order image, I_3**.** of the receiver antenna in wall 3 is found. Then, the second order image, at point is found by reflecting the first order image in the semi-intinite plane containing wall 4. Finally, the co-ordinates of the highest order image, at point $I_{3,4,2}$. are found by reflecting $I_{3,4}$ in wall 2. Once all the images have been found, the complete path and all the reflection points can be found as shown in Fig. 5. The signal strength of this propagation path can then be calculated using eqn. 10.

(b) ***Brute-force rayfracing method:***[17] This method accounts for all possible propagation paths. The transmitters and receivers are modelled as points at discrete locations in three-dimensional space. All the possible angles of departure and arrival at the transmitters and receivers are considered to determine all possible rays that may leave the transmitter and arrive at the receiver. Ray tracing is accomplished by an exhaustive search of a ray tree taking into acco.int decomposition of the ray at each planar intersection. First the model determines whether a line-of-sight path exists and if so computes the received signal. Next, the model traces a source ray in a specified direction and detects whether an object intersection occurs. If no intersection is found,

the process stops and a new source ray in a direction making an angle with the original ray is initiated. Once an intersection has occurred, a check is made to see whether the ray can be considered to have reached any of the specified receiver locations. If the ray is found to reach a receiver location, the received signal is computed. After checking the reception, the incident ray is divided into a transmitted and a reflected ray, each of which is traced to the next intersection in the same way. This recursion continues until the ray intensity falls below a specified threshold or no further intersections occur.

As multiple scattering of a ray will not contribute significantly to the received power since the amplitude of these scattered rays decreases rapidly with distance, the existing ray-tracing models using this approach do not include multiple scattering and also do not trace scattered rays recursively. At each step in the creation of a ray tree, the corresponding ray segment is tested to see whether it can be considered to have reached specified receiving locations. To do this, a reception sphere is constructed about the receiving location with a radius proportional to the unfolded path length from transmitter to receiver and the angular spacing between neighbouring rays at the source. If the ray intersects the sphere, the ray is taken as contributing to the received signal. Otherwise, the ray is treated as not having reached the receiver location.

The reception sphere effectively accounts for the divergence of the rays from the source. For sufficiently small ray separation 0**,** ray intercepting the sphere will be an accurate measure of the ray that would pass directly through the receiving point, The physical interpretation of the reception sphere can be justified with the aid of Fig. 6.

This Figure is a two-dimensional representation of a ray being traced. Two adjacent rays launched at $\pm u$ relative to the test ray are also shown. Note that in three dimensions any ray will have more than two adjacent rays and angular separation of the adjacent rays will not necessarily coincide with the co-ordinate axes. As shown in Fig. 7, a reception sphere with the correct radius $\approx u\mathrm{d}/2$ can receive exactly one of the rays. If the radius is too large. Two of the rays could be received and would, in effect, count the same ray path twice. Likewise, if the radius is too small, it is possible that none of the rays will intercept the sphere and the ray path energy will be excluded. The path loss error due to perceiving two rays would be a few decibels. A missed specular ray could lead to a much larger error if a significant amount of energy is carried by that ray.

5. Conclusion

In this paper, we have pointed out the importance of propagation models in the development of indoor wireless communications. Propagation models provide reliable and easy way for estimation of signal strength and time dispersion in many indoor environments. These data are valuable and can facilitate the process of design and installation of the developed System for monitoring and management of energy efficiency in public buildings using radio communications.

Acknowledgment

This paper was supported under Project Nr DUNK-01/03.12.09 "University Scientific and Research Complex for Innovation and Transfer of Knowledge in Areas of Micro / Nano Technologies and Materials, Power Effectiveness and Virtual Engineering".

References

1. Altimirski E., N. Kaloyanov, P. Vichev, V. Plamenov, 'System for monitoring and management of energy efficiency in public buildings' ICEST 2013 Ohrid, Macedonia
2. Tam W. K., V.N. Tran, 'Propagation modeling for indoor wireless communication', Electronics & Communication Engeneering Journal, October 1995.
3. Saleh. A., and Valenzuela, RA.: 'A statistical model lor indoor multipath propagation', *IEEE J. Sel. Areas Commun.,* February 1987, SAC-5, (2), pp.12&137
4. Bultitude, R.J.: 'Measurement, characterization and modeling of indoor 800/900 MHz radio channels for digital communications', *IEEE Commun. Mag.,* June 1987, 25, (6). pp.5-12
5. Owen, F.C., and PUNDEY, C.D.: 'In-building propagation at 900 MHz and 1650 MHz lor digital cordless telephone'. 6th Int. Conf. on Antennas and Propagation, ICAP 89, Part 2: Propagation, 1989, pp.276-281
6. Alexander, SE.: 'Characterizing buildings for propagation at 900 MHz', *Electron. Lett.,* September 1983. 19, (20). p.860
7. Alexander, SE: "The propagation of radio signals at 900 MHz within buildings'. IEE Colloquium Digest 1986/030, 'Propagation in confined spaces and tunnels', IEE, London, UK 1986, pp.7/1-7/4
8. Turin. G.L.: 'Communication through noisy, random multipath channels'. 1956 IRE Convention Rec., part 4, pp. 154-166
9. Turin.G.L.,Clapp,F.D.,Johnston,T.L.,Fine,S.B.,and Lavry. D.: 'A statistical model of urban ultipath propagation', *IEEE Trans. Veh. Technol.,* February 1972, VT-21, pp.1-9
10. HAShemi, H., Tholl. D., and Morrison, G.: 'Statistical modeling of the indoor radio propagation channel part I'. Proc. IEEE Vehicular Technology Conference, WC'92, Denver, CO, May 1992, pp.33&342
11. Hashemi, H.: 'Impulse response modelling of indoor radio propagation channels', *IEEE J. Sel. Areas Commun.* September 1993, SAC-1 1, pp.1788-1796
12. Keenan, J.M.. and Motley, AJ.: 'Radio coverage in buildings', *Er. Telerom. Technol. J.*. January 1990, 8, (l), pp.19-24
13. Seidel, S.Y., and Rappaport, T.S.: '914 MHz path loss prediction models for indoor wireless communications in multiflorous buildings', *IEEE Trans. Antennas & Propagation.* February 1992, AP-40, (2). pp.207-217
14. Valenzuela, RA: 'A ray tracing approach to predicting indoor wireless transmission'. Proc. 43rd IEEE Vehicular Technology Conference, NJ. USA, 1993, pp.214-218
15. Laurenson, D.I., She1kh.A.U.H.. and Mclaughlin. S.: 'Characterization of the indoor mobile channel using a ray tracing technique'. Proc. 1992 IEEE Int. Conf. on Selected Topics in Wireless Communications, Vancouver, BC, 25th-26th June 1992, pp.6568
16. Mckown, J.W., and Hamilton, R.L.: 'Ray tracing as a design tool for radio networks'. *IEEE Network,* Nov. 95.
17. Seidel, S.Y., and Rappap0rt.T.S.: 'A ray tracing technique to predict path loss and delay spread inside buildings'. Proc IEEE GLOBECOM '92 Conference, Orlando, USA, 6th-9th December, 1992, pp.649-653

Author Index

AUTHOR INDEX

ISRSSP 2013

Proceedings of ISRSSP 2013
Third International Symposium on Radio Systems and Space Plasma
ISBN: 978-619-90124-1-3